Evaluating Ocean Oxygenation: A Redox Study of Middle Ordovician Carbonates

Brenna Henderson
Advisor: Dr. Alan Jay Kaufman
Co-Advisors: Matt Pedersen, Tian Gan
December 2nd, 2025

University of Maryland, College Park, Maryland, USA
GEOL394

Table of Contents

Abstract

The Paleozoic Era contains two significant biogenic radiations, although the cause of these 'explosions' remains inconclusive. The Great Ordovician Biodiversification Event (GOBE) occurred some 40 million years after the Cambrian Explosion of animals, replacing the earlier faunas with a wide variety of suspension feeders and pelagic animals. Middle Ordovician carbonates near Strasburg, Virginia, preserve the steep onset of the GOBE (Read, J. & Repetski, J., 2012) and consist of organic-rich limestones and shales from supratidal to deep subtidal and continental slope depositional environments. This study aims to use carbonate redox proxies to explore changes in marine oxidation states as a possible cause of the GOBE. Uranium is a proxy for global oxygenation states as it has a long residence time in the oceans and is unique among most other metals in seawater, given that it is soluble when oxidized. In contrast, cerium anomalies (Ce/Ce*) reflect local redox conditions, with studies indicating oxic conditions when the ratio is < 1 and reduced conditions when the ratio is > 1. Sulfur isotope compositions in acidified residues are used to assess seawater sulfate abundance and rates of microbial sulfate reduction, a process that occurs under anaerobic conditions. Additionally, organic matter and carbonate carbon isotope compositions are analyzed to track the balance between organic carbon burial and oxidation through the Middle Ordovician. Elemental ratios and oxygen isotope compositions are used to assess diagenesis or contamination in the samples. Data from the Strasburg section include $\delta^{13}C_{org}$, $\delta^{13}C_{carb}$, $\delta^{18}O$, $\delta^{15}N$, and $\delta^{238}U$ measurements. The $\delta^{238}U$ values are significantly lower than modern seawater, suggesting a more reducing global ocean during the Middle Ordovician. The $\delta^{13}C_{carb}$ values remain slightly positive, indicating modest organic carbon burial, while the $\delta^{18}O$ values are consistent and slightly lighter than modern. $\delta^{13}C_{org}$ data show evidence for local redox fluctuations, while $\delta^{15}N$ values are variable and quite enriched. Overall, results suggest that oceans were widely anoxic during the Great Ordovician Biodiversification Event, and therefore, do not support oxygenation as a driving factor of the GOBE.

Plain Text Abstract

The Ordovician is a geological period far back in Earth's history, ranging in age between 487 and 443 million years ago. Marine animal life diversified rapidly during this period, creating complex ecosystems that parallel those of modern oceans. Many hypotheses have been proposed to explain this biological explosion, and this study explores the hypothesis that a rise in oxygen was the driving factor. I will test a series of Ordovician carbonate rocks from central Virginia that were deposited in various water depths for the uranium that is incorporated from seawater when they formed. Uranium is a heavy (and radioactive) element that is useful for understanding the amount of oxygen in seawater around the globe. In ocean water rich in oxygen, as it is today, uranium will stay dissolved, but in seawater lacking oxygen, uranium will get buried with minerals into sediments. Thus, by measuring a range of uranium compositions in carbonate rocks, I will evaluate how much oxygen was in Ordovician oceans. All animals need oxygen to survive, so analyzing how much oxygen was present in Ordovician seawater could provide key information about the explosion of animal life at this time.

Introduction

The Ordovician Period (from 485 to 443 Ma) is marked by major tectonic, climatic, and biological transformations. Associated with high CO_2, temperatures in the Early and Middle Ordovician were warm but progressively cooled, leading to a glaciation at the end of the period (Marcilly et al., 2022). The short-lived Hirnantian glaciation at ca. 460 Ma is the earliest known Paleozoic ice age and is associated with a mass extinction that resulted in the death of 85% of marine species (Sheehan, 2001). The Ordovician also marks the earliest evidence of non-vascular land plants, such as algae and bryophytes (Steemans et al., 2009; Wellman & Gray, 2000). The spread of non-vascular land plants may have played a role in an increase of oxygen and a decrease of CO_2 in the atmosphere, leading to the ice age (Lenton et al., 2012). The seas during this period were characterized by high calcite saturation levels such that marine organisms with low-magnesium calcite shells predominated (Jones et al., 2019). The carbon cycle in the Ordovician had multiple positive excursions that reflected changing biodiversity and climate. For example, positive shifts in $\delta^{13}C$ values were likely caused by an increase in organic carbon burial that could have contributed to global cooling (Men et al., 2022). Major tectonic events associated with the assembly of Gondwana were also occurring at this time. The Taconic Orogeny along the eastern seaboard of Laurentia, which started in the Cambrian and continued through the Ordovician, influenced sediment supply and shelf geometry with the erosion of newly formed highlands contributing siliciclastic material to adjacent basins. High levels of volcanic activity during this time led to the deposition of K-bentonite ash layers as well as episodic increases in atmospheric CO_2 and temperature.

The Ordovician is also characterized by the Great Ordovician Biodiversification Event (GOBE). While many new phyla appeared during the Cambrian, the diversity of animal taxa exploded during the Middle Ordovician. Ecosystems became robust and expanded into new

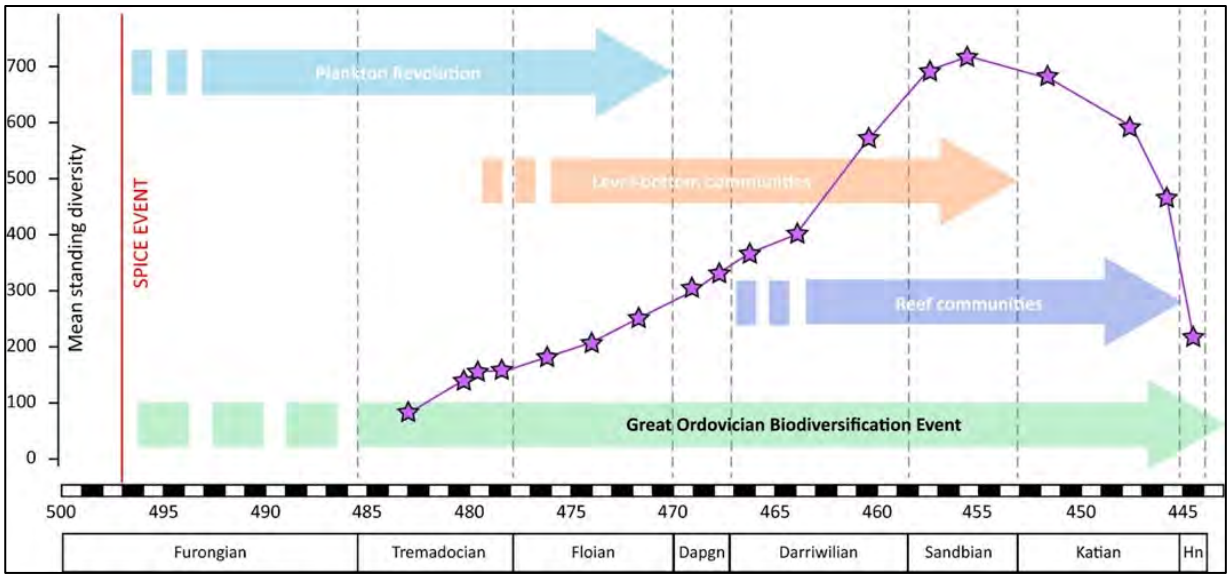

Figure 1. An illustration of the increase in mean standing diversity (number of species) throughout the Great Ordovician Biodiversification Event. Although the increase in the reef, plankton, and benthic communities occurred at separate times, they are linked together and are accepted as one event. The SPICE event is a notable positive carbon isotope excursion in the late Cambrian Period (Dahl et al., 2014). The data was produced using the Paleobiology Database to compile 400 different references of Ordovician formations, including near Strasburg, Virgina. The purple stars represent data compiled by Kröger & Lintulaakso (2017) and presented by Servais & Harper (2018).

environments as plankton, benthic, and reef communities flourished (Figure 1). Phytoplankton diversity and abundance increased steadily in the Ordovician (termed the plankton radiation) pelagic realm, while brachiopods and echinoderms were the most influential of the benthic communities and bryozoans and sponges dominated reefs (Servais & Harper, 2018). The Ordovician also saw an increase in predators and complex food chains (Sperling et al., 2013). The notable increase in biological diversity was global in scope and may have lasted as long as 20 Ma (Servais et al., 2010).

Hypothesis

This study investigates the potential causal link between ocean oxygenation and the GOBE by analyzing carbonate uranium isotopes ($\delta^{238}U$) believed to be a global redox proxy and cerium anomalies (Ce/Ce*) that reflect local oxidation states of seawater. In addition, carbon, oxygen, and sulfur isotopes of carbonate, organic matter, and nitrogen were determined in a suite of Middle Ordovician sedimentary rocks near Strasburg, VA. Understanding whether the rise of oxygen in the early Paleozoic led to the GOBE may also provide insight into how deoxygenation of ecosystems due to climate change may impact modern environments.

The null hypothesis is that redox states indicated by uranium isotopes and cerium anomalies in carbonate proxies will show **no change** in marine oxygen levels in the Middle Ordovician relative to times before and after the event. This outcome would suggest that factors other than oxygen play a more important role in driving animal diversification. The primary working hypothesis is that marine oxygen levels **increased** in the Middle Ordovician as monitored by a rise in carbonate uranium isotope compositions. A secondary working hypothesis is that the oxygenation states of Middle Ordovician oceans **decreased** as reflected in a decline in carbonate uranium isotope compositions. Anoxic oceanic conditions during the GOBE would challenge the causal link between oxygen and biodiversification.

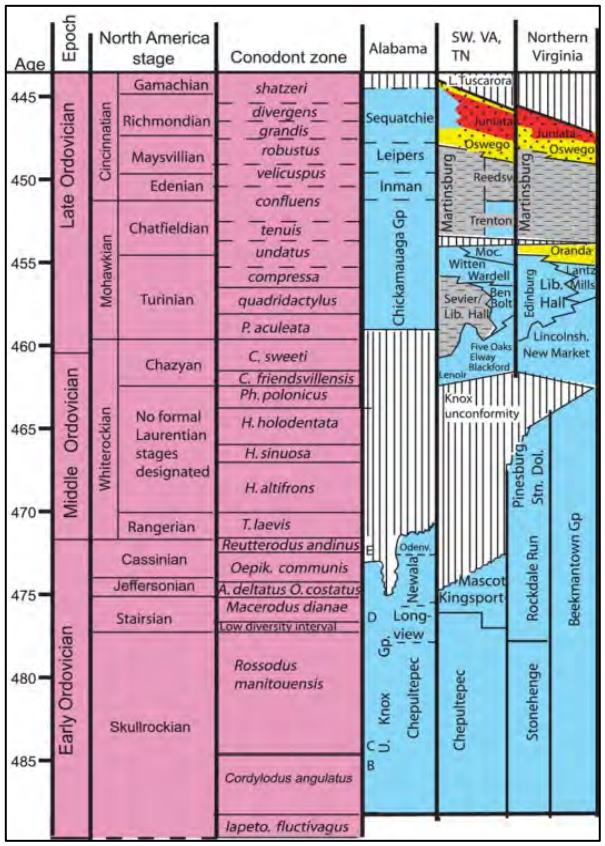

Figure 2. A chronostratigraphic diagram showing the North American stages of the Ordovician Period with broadly correlative units in eastern Laurentia illustrated and highlighting the Knox unconformity. Conodont zone refers to the main conodont fossils found in that time interval (after Read and Repetski, 2012).

Geologic Setting

Samples used in this study were collected near Strasburg, VA, along Battlefield Road, the site of a Civil War skirmish (Appendix, A-1). These marine carbonates were deposited in the Middle-Late Ordovician, representing the Beekmantown Group and New Market, Lincolnshire, and Edinburg Formations (Figure 2). The dolomitic Beekmantown Group is separated from the overlying limestone-dominated succession by the Knox unconformity (Figure 3), representing

a period of continental exposure associated with a relative sea-level fall that may have resulted from plate uplift during tectonic collision from Laurentia, Baltica, and Siberia (Torsvik & Cocks, 2017; Webby et al., 2004; Scotese, 2023). Unconformities represent intervals of missing time, exposure, erosion, and potential diagenetic overprinting of the underlying facies, all of which can influence preservation of carbonates and their isotopic signatures. Their presence can mark shifts in depositional regime or sea level change that are relevant when correlating isotope excursions. Beekmantown sedimentary rocks are primarily shallow marine dolomites containing thin shale intervals that have been regionally karstified. Similar to unconformities, the occurrence of dolomite is critical since dolomitization alters both the mineralogy and geochemistry of carbonates. Primary dolomite can record seawater chemistry, but secondary dolomite typically forms during burial or fluid flow events and can reset or partially alter original isotope values. Both primary and secondary dolomite have been known to occur in the Beekmantown Formation (Kolkas & Friedman, 2001). The dolomitization here was likely driven by microbial activity and early diagenesis. At low temperatures, magnesium ions resist incorporation into carbonates due to their hydration shells, but microbial extracellular polymeric substances can strip these shells and create favorable nucleation sites (Sharp, 2007). Later dolomite likely formed during burial, where temperature and fluid flow helped overcome such kinetic barriers. Above the Knox unconformity lies the supratidal to peritidal New Market Formation (Figure 4), which is predominantly a light grey limestone with fenestrae that may represent calcite replacement of soluble evaporite minerals. The bedding is an alternation of thick and thin massive, microbial, and fossiliferous layers. The Lincolnshire Formation disconformity overlies the New Market Formation (Figure 4) and is mainly composed of subtidal dark grey ribbon limestone likely of a turbiditic origin, packed with black chert nodules, as well as fossiliferous bioherms that include microbial oncolites, gastropods, brachiopods, bryozoan, trilobites, and sponges. The formation is further characterized by the presence of en echelon fractures formed from tectonic bending of the plate within the foreland basin setting. Shale layers thicken near the top of the Lincolnshire Formation, with a thick silicified shale horizon at the very top of the interval. Silicification may

Figure 3. A view of the contact between Beekmantown dolomite (lower) and New Market limestone (higher) representing the Knox unconformity (highlighted in red) at Tumbling Run below Battlefield Road. Taken at Battlefield Road in spring 2025.

Figure 4. A roadside view of the New Market (right) and Lincolnshire (left). The formations are separated by an unconformity, highlighted by a red line. Taken at Battlefield Road in spring 2025.

Figure 5. A view of the alternating shale and nodular carbonate beds that make up the Edinburg Formation. Taken at Battlefield Road in spring 2025.

be related to devitrification of a K-bentonite layer immediately below the shale. The ash was likely the result of an eruption from an approaching volcanic arc. Deep subtidal to slope facies mixed nodular limestone and shale of the Edinburg Formation (Figure 5) gradually transitions into thickly bedded limestone facies near the top of the measured section. The increase of siliciclastic material in the basal Edinburg Formation is notable and likely associated with weathering of the volcanic highland (Read and Repetski, 2012).

Ordovician Environments

The oceans during the Ordovician started with warm temperatures (~40 ºC) but cooled throughout the period, leading to a glaciation in Late Ordovician that is associated with a mass extinction (Servais & Harper, 2018; Bergmann et al., 2025; Harper, 2023). Long-term Ordovician cooling may have played a role in seawater oxygenation insofar as the solubility of the breathing gas increases with lower temperatures. As animals need oxygen for respiration, a decrease in temperature and an increase in dissolved oxygen could provide ideal conditions for animal diversification during the GOBE. The cause of this cooling is hypothesized to be tectonic in origin by increasing weathering and sedimentation rates that bury photosynthetic organic

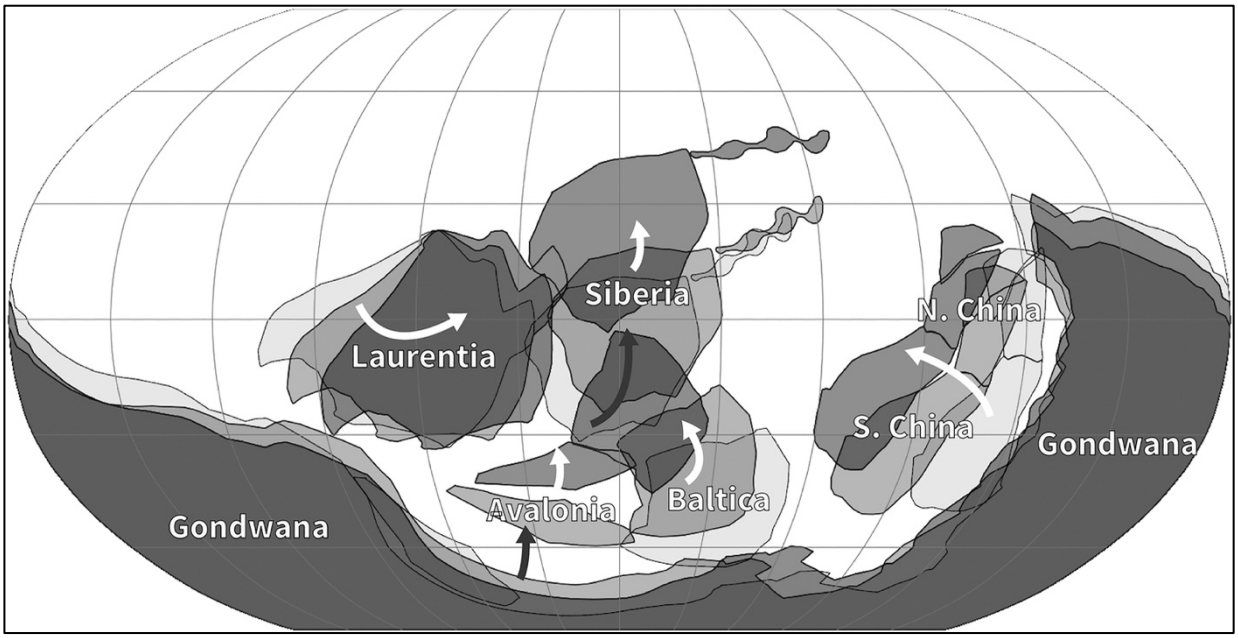

Figure 6. Continental movements during the Ordovician period, visually illustrated by Scotese (2023). Laurentia and Baltica rotated counterclockwise and drifted northward, while Gondwana stayed near the South Pole with slower movement. Arrows show the direction and speed of plate motion. A new subduction zone beneath Laurentia later sped up tectonic activity during the Late Ordovician.

matter produced in the oceans by high nutrient concentrations (Bergmann et al., 2025). Earth's temperature has primarily been influenced by the presence of CO_2 in the atmosphere, with the reaction of chemical weathering removing CO_2 and volcanic activity adding CO_2 to the atmosphere. The Middle Ordovician interval was marked by episodic volcanism, shown by thick ash deposits (Servais et al., 2010), including the K-bentonite preserved in the studied succession. Temperatures may have increased during volcanic episodes but then quickly dropped due to consumption of CO_2 during silicate weathering of the newly exposed volcanic rocks, which account for 33% of CO_2 consumption today (Nardin et al., 2011). Ordovician tectonic activity

(Taconic Orogeny) was likely associated with the closing of the Iapetus Ocean (Stillman, 1984; Staal & Hatcher, 2010) between Laurentia and one or more volcanic island arcs (Figure 6). Studies have been conducted that propose a causal link between an increase in tectonic activity and the growth of biodiversity (Miller & Mao, 1995). Orogenesis drove uplift, weathering, and erosion, which consumed atmospheric CO_2 and led to surface refrigeration. As temperature fell and dissolved oxygen increased through the burial of photosynthetic organic matter, it is plausible that ventilation of the oceans was the driving force for the GOBE.

Systematics of Geochemical Proxies

Diagenetic Alteration

When biogenic carbonates, such as the New Market limestones, interact with diagenetic fluids moving through the sediment after burial, those fluids can alter the isotope ratios, such as $\delta^{238}U$, $\delta^{18}O$, and $\delta^{13}C$. The more fluid that moves through the rock, the more likely it is that the original isotopic signal gets modified (O'Neil, 1977). There are two main diagenetic processes that change isotopes: cementation and recrystallization. Cementation occurs as new carbonate grows in pores between grains, usually in high-energy environments. When unstable carbonate minerals dissolve and reprecipitate as a more stable mineral, it is called recrystallisation. This process can alter the isotopes in the carbonate and equilibrate with the fluid it's interacting with. However, this process depends on temperature, isotopic composition of the fluid, how much fluid is available, and mineral stability. Early marine cements could preserve the original signal, but later freshwater or cement alterations could lower $\delta^{18}O$ and $\delta^{13}C$ values. In carbonate minerals, $\delta^{18}O$ is the most vulnerable to resetting during burial, fluid-rock interaction, or meteoric water infiltration, often resulting in systematically lighter values due to exchange with isotopically depleted diagenetic fluids. $\delta^{13}C_{carb}$, in contrast, is generally more resistant to post-depositional alteration. $\delta^{13}C_{org}$ and $\delta^{15}N$ values in organic matter are also susceptible to alteration, especially when total organic carbon (TOC) or total nitrogen (TN) is low, or when diagenetic oxidation of organic material occurs (Swart, 2015). Diagenetic processes also influence $\delta^{238}U$ as U isotopes can be overprinted by changes in pore water redox conditions or by recrystallization, often leading to elevated uranium isotopic signatures due to U(IV) enrichment under reducing conditions (Romaniello et al., 2013). Additionally, REEs may be redistributed during freshwater alteration; however, cerium is more robust to diagenetic overprinting than many other redox proxies since it is often immobilized early under oxic conditions (Sharp, 2007).

Uranium Isotopes

Uranium isotopes (U) serve as a global redox proxy as uranium is soluble under oxidizing conditions, but under reducing ones, partitions into euxinic reservoirs causing isotopic redistribution. Uranium's long residence time of ~400,000 years (Ku et al., 1977), relative to the ocean's mixing time of ~1,500 years, ensures homogeneous concentration and isotopic distribution. In oxic environments, uranium exists predominantly as soluble U^{6+} that stays in solution. In anoxic settings, however, U^{6+} is reduced to insoluble U^{4+}, which is primarily sequestered in euxinic facies and is preferentially enriched in the heavier ^{238}U isotope. Sequestration of the heavy isotope leaves seawater progressively enriched in the light ^{235}U isotope thereby resulting in lower $\delta^{238}U$ values in carbonates (Figure 7). Modern seawater exhibits a $\delta^{238}U$ value of approximately -0.38‰ (Kipp et al., 2022). Values similar to this in Ordovician carbonates would indicate a well-oxygenated environment. $\delta^{238}U$ is defined as:

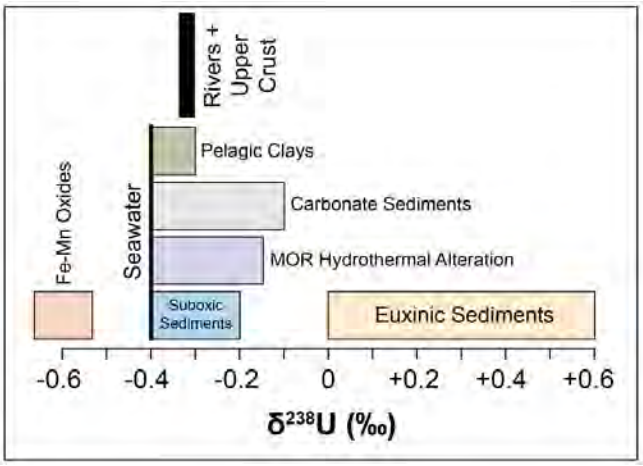

Figure 7. Mass balance model illustrating the primary sinks for seawater uranium and their isotopic compositions. Euxinic sediments represent the largest and most isotopically fractionating sink (Tissot and Dauphas, 2015).

$$\delta^{238}\mathrm{U} = \left(\frac{\frac{^{238}\mathrm{U}}{^{235}\mathrm{U}}\ sample}{\frac{^{238}\mathrm{U}}{^{235}\mathrm{U}}\ standard} - 1 \right) * 1000.$$

Cerium Anomalies

Rare earth elements (REE) are chemically similar elements that include the redox proxy cerium (Ce). Unlike uranium, cerium anomalies in marine carbonates act as local redox proxies due to a short residence time of ~100 years (Tazoe et al., 2007). Under oxic conditions, Ce^{3+} is oxidized to Ce^{4+}, which bonds onto iron and manganese oxides, getting buried in carbonates and, therefore, removed from seawater, creating a negative Ce anomaly ($Ce/Ce^* < 0.9$). In anoxic environments, Ce remains in its soluble Ce^{3+} form, leading to no depletion and resulting in a positive Ce anomaly ($Ce/Ce^* > 1.0$). Cerium anomalies were previously calculated using the conventional La-Pr normalization approach; however, this method is sensitive to anomalous La behavior, which can artificially amplify the Ce anomaly. For this reason, the La independent method of Lawrence et al. (2006) and Tostevin et al. (2016) is used in this study. Ce/Ce^* is defined as:

$$\frac{\mathrm{Ce}}{\mathrm{Ce}*} = \frac{\mathrm{Ce}}{\frac{Pr^2}{Nd}}.$$

Carbonate Carbon Isotopes

Carbon isotope compositions of marine carbonates are generally thought to reflect the proportional burial of carbonate and organic matter in sedimentary archives (Hayes, 1993). Increased burial of organic carbon (the small fraction of primary photosynthetic production that avoids remineralization back to CO_2) that is enriched in ^{12}C leaves the dissolved inorganic carbon (DIC) pool progressively enriched in ^{13}C, resulting in more positive $\delta^{13}C$ values in carbonate sediments and rocks. On the other hand, enhanced oxidation of photosynthetic organic matter (to carbonate ion) releases ^{12}C back into the DIC pool, leading to more negative $\delta^{13}C$ values in carbonates (Mackensen & Schmiedl, 2019). $\delta^{13}C$ is defined as:

$$\delta^{13}\mathrm{C} = \left(\frac{\frac{^{13}\mathrm{C}}{^{12}\mathrm{C}}\ sample}{\frac{^{13}\mathrm{C}}{^{12}\mathrm{C}}\ standard} - 1 \right) * 1000.$$

Carbonate carbon isotopes will primarily be used to define time-series trends through the succession and to locate positive anomalies that are noted in Middle Ordovician carbonates worldwide for correlation purposes. Carbonate carbon isotopes can also reflect global biogeochemical cycling and productivity.

Total Organic Carbon Abundance and Isotopes

A comparison of organic richness is made between each studied unit, which may be related to the depositional environment and magnitude of primary productivity. Water column redox conditions also have an essential impact. If bottom waters are anoxic, anaerobic microbes can consume the organic matter formed in the water column by photosynthesizers. In doing so, they imprint their own isotopic signal on preserved organic matter, modifying the original $\delta^{13}C_{org}$ values recorded in the sediment. Isotope abundances may track with those of carbonate carbon isotopes, supporting time-series trends as being primary in origin (Edwards & Saltzman, 2016). Alternatively, the organic carbon isotope composition may inform about the source of the organic matter in the depositional environment.

Nitrogen Isotopes

Nitrogen isotopes can reflect the amount of oxygen present in the water column through a process called denitrification. Denitrifying bacteria live only in anoxic environments and, when active, take nitrate from the water column and convert it to N_2 gas, which escapes into the atmosphere. The enzyme related to denitrification preferentially uses the light isotope, and hence the product N^2 is depleted, leaving seawater nitrate progressively enriched. The nitrate left behind in the water column becomes enriched in the heavier ^{15}N. This enriched nitrate is then incorporated into organic matter sinking to the seafloor. Therefore, high $\delta^{15}N$ values would reflect anoxic conditions. $\delta^{15}N$ is defined as:

$$\delta^{15}\mathrm{N} = \left(\frac{\frac{^{15}\mathrm{N}}{^{14}\mathrm{N}}\ sample}{\frac{^{15}\mathrm{N}}{^{14}\mathrm{N}}\ standard} - 1 \right) * 1000.$$

Pyrite Sulfur Isotopes

Sulfur isotope compositions of pyrite preserved in marine carbonates may be used as an indicator of oxygen content and of microbial activity insofar as microbial sulfate reducers are obligate anaerobes (they cannot live in oxygenated seawater). The addition of sulfate to oceans is primarily due to the weathering of sulfur-bearing minerals. On the other hand, the burial of sulfur-bearing minerals leads to sulfate removal. A process called microbial sulfate reduction (MSR) occurs when microbes convert sulfate to hydrogen sulfide and produce pyrite. The pyrite is generally enriched in ^{32}S if the sulfate reservoir of the oceans is large and the metabolic rate is slow. Under these conditions and when the mineral is buried in sediments, seawater becomes progressively enriched in ^{34}S and oxygen is released into the atmosphere (Gomes et al., 2021). On the other hand, when pyrite on land is oxidized, oxygen in the atmosphere is removed. Since MSR can only occur in anoxic environments, $\delta^{34}S$ also provides insight into the oxygen content in marine systems (Li et al., 2022). $\delta^{34}S$ is defined as:

$$\delta^{34}S = \left(\frac{\frac{^{34}S}{^{32}S}\ sample}{\frac{^{34}S}{^{32}S}\ standard} - 1 \right) * 1000.$$

Oxygen Isotopes

Oxygen isotope compositions in recent marine carbonates can be used as indicators of seawater temperature or climate conditions. During cold climate intervals, seawater becomes enriched in ^{18}O due to the preferential storage of ^{16}O in ice on land, resulting in higher $\delta^{18}O$ values in seawater. Previous $\delta^{18}O$ data in well-preserved Ordovician brachiopods have revealed trends of increasing values (Veizer et al., 1999). However, bulk sediment oxygen isotope compositions are usually more effective for identifying alteration. Freshwater is typically more isotopically depleted than marine water. If freshwater interacts with marine carbonates, it can shift the $\delta^{18}O$ signature to more negative values. On the other hand, extreme evaporation would result in ^{18}O enrichment (Epstein et al., 1951). $\delta^{18}O$ is defined as:

$$\delta^{18}O = \left(\frac{\frac{^{18}O}{^{16}O}\ sample}{\frac{^{18}O}{^{16}O}\ standard} - 1 \right) * 1000.$$

Methods

Sample Preparation

Samples were collected on Battlefield Road near Strasburg, VA. Dr. Alan Jay Kaufman and colleagues from Ohio State University collected samples in 2021, and 19 additional samples were collected in 2025 by Dr. Kaufman and me. Each sample was cut into two slabs using the MK tile saw in the rock-cutting facility. One slab was finely polished using a Struers Labopol grinding wheel and 80, 220, 320, and 500 grit pads to identify fine-grained phases free of secondary veins and surface weathering for microdrilling. The other slab had both surfaces and weathered edges ground before crushing using an agate mortar and pestle to avoid contact with

metals. Empty 50 mL plastic centrifuge tubes were weighed and filled with approximately 1.5 g of the powdered sample. This method follows that of Cui et al. (2015).

Uranium Analysis

Uranium concentration determination is required to know how much double spike (solution that contains two enriched isotopes of uranium in known proportions) is to be added to the solution for isotope dilution and mass bias correction and how much solution is necessary to dry down to obtain 300 ng of uranium for the isotope measurements. To start, a 0.1 mL aliquot is taken from the decanted solution (see sample preparation above) and is diluted 10-fold with 0.4 mL of 2% HNO_3 and 0.5 mL of the internal standard. Standards are diluted with 200 ppb Bi and run along with the samples in the Element 2 inductively coupled plasma mass spectrometer (ICP-MS) at the University of Maryland Plasma Lab. Before measurement, the Element 2 ICP-MS is run with blanks of 2% nitric acid. The blanks are run every five to six samples to determine and subtract background concentrations. Raw intensities are given from the instrument measurements and are corrected by completing a blank subtraction. An internal standard correction (normalized Bi concentrations to the Bi concentration of the first standard measured) accounts for drift during the analytical session. There is an assumption that the standard intensities directly correspond to known concentrations. A calibration curve is plotted to gather an equation for the intensities and concentrations in ppb. Using this equation, the measured concentrations are calculated and multiplied by ten to account for sample dilution. The uranium concentration, mass of uranium, and amount of sample to dry down are calculated in Excel based on these values and the weights of the solutions and powers (Appendix A-2). Supernatants were dried down in Teflon beakers at 180 °C, spiked with a calibrated amount of U^{233}/U^{236} double spike, and digested in reverse aqua regia to ensure complete dissolution. The partially dried samples were then taken through successive digestions with concentrated HNO_3 and HNO_3/H_2O_2 to remove organics and convert them into a 3 M HNO_3 matrix suitable for UTEVA column chemistry. Uranium purification was achieved using UTEVA resin, including resin cleaning, equilibration, loading of the 3 M HNO_3 sample, rinsing of matrix elements, conversion to chloride, and leaching of U in 0.05 M HCl. A second purification was performed on DGA resin to remove remaining matrix elements. The final purified U fraction was dried down, redissolved in 2% HNO_3 to a concentration of 50 ppb, and transferred to acid-cleaned centrifuge tubes for measurement on the Neptune ICP-MS. This method is based on Tissot and Dauphas (2015).

Rare Earth Element Analysis

The initial crushed powder was weighed to 25 mg and put inside a centrifuge tube. The samples were then rinsed with Milli-Q water and centrifuged. The Milli-Q water was decanted, and 312.5 mL of 2% HNO_3 was added. The sample was agitated and set out overnight. After centrifuging, the solution was decanted, and 625 mL of 2% HNO_3 was added. The sample was again agitated and set out overnight. The sample was centrifuged and decanted into a fresh 15 mL centrifuge tube. After being diluted with 10 mL of 2% HNO_3, the samples were put into the ICP-MS at the University of Maryland for analysis. This method is based on Tostevin et al. (2016).

Organic Matter Carbon Isotope Analysis

For carbon isotope analysis by gas source mass spectrometry (GSMS) in the UMD Paleoclimate CoLaboratory**,** between 0.5-2.0 mg of the residue was weighed**,** depending on the color (a rough indicator of organic matter content)**,** into 3x5 mm tin cups. Approximately 0.2 mg of the urea standard was also weighed and placed into the tin cups for system suitability tests and to calculate uncertainties with the instrumental measurements. The samples and urea were combusted with a Eurovector elemental analyzer (containing an oxidation column filled with chromium oxide and cobaltous-cobaltic oxide at 1040 ºC and a reduction column filled with elemental copper wire at 650 ºC) with the resulting CO_2 (and N_2) pushed through a Mg-perchlorate water trap and then into the source of a continuous flow Multicollector Isoprime GSMS in a stream of UHP (ultra-high purity) helium gas. Some samples were run multiple times to achieve peak heights of greater than four nanoampere, which provides the most accurate determinations. The carbon isotope offset from the true value of the urea standard was applied to the raw sample measurements to determine their final values. Based on the wt% of organic carbon in the residue and the %carbonate in the sample, the percent total organic carbon (%TOC) was calculated (Appendix A-3).

Carbonate Carbon and Oxygen Isotope Methods

Rock slabs were cut, polished, photographed, and micro-drilled to isolate fresh carbonate powders. Analyses were carried out on a Multiflow Isoprime gas-source mass spectrometer. All $\delta^{13}C_{carb}$ and $\delta^{18}O_{carb}$ values were normalized to the VPDB scale using a two-point calibration defined by standards JTB-1 and MCC.

Nitrogen Isotope Methods

Residues obtained through 3 M HCl acidification were dried and submitted for nitrogen isotope analysis. The residues represent the insoluble organic fraction following carbonate removal. The residue reacted overnight, was rinsed threefold with MQ-water, and dried at 80 °C. These residues were then analyzed for $\delta^{15}N$ on the Multicollector Isoprime GSMS in the UMD Paleoclimate CoLaboratory.

Results

Uranium, Carbonate Carbon, and Oxygen

The dataset of $\delta^{238}U$, $\delta^{13}C_{carb}$, and $\delta^{16}O$ was compiled and tabulated in Excel and visually illustrated in Figure 8. The datum is presented alongside a stratigraphic section, enabling comparison between geochemical signatures and depositional facies across the Beekmantown, New Market, Lincolnshire, and Edinburg Formations. In the $\delta^{13}C_{carb}$ panel, values range from around -3.5‰ to +1.0‰. The curve shifts gradually upward through the section, with several intervals of relative enrichment or depletion, but overall, the points lie close together with a smooth progression. The dashed line at 0‰ serves as a visual reference for comparison to marine carbonate compositions. The $\delta^{18}O$ panel shows values between roughly -9.7‰ and -6.1‰. These points form a continuous vertical trend beyond the initial increase around the unconformity. The $\delta^{238}U$ panel displays values from approximately -0.9‰ to -0.2‰. These values are shown alongside reference lines: the dotted vertical line at 0.4‰, representing the modern Bahamian

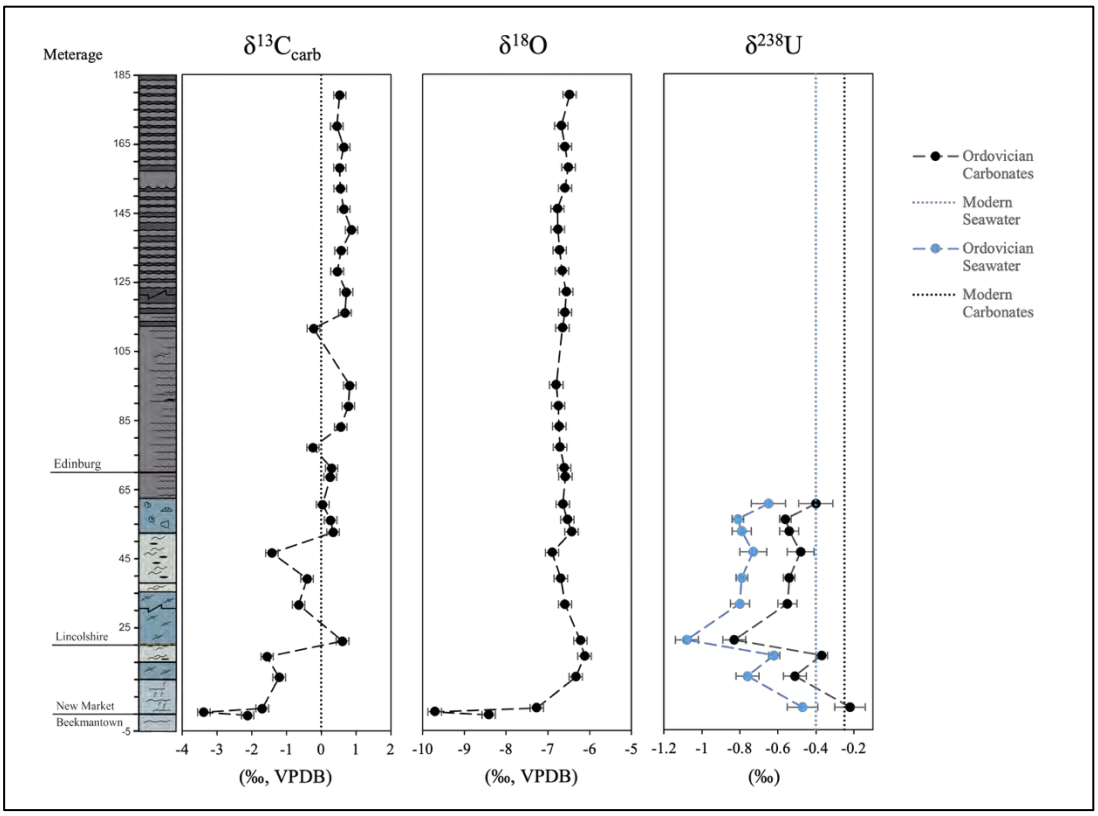

Figure 8. Chemostratigraphic plot showing the correlations between $\delta^{238}U$, $\delta^{13}C_{carb}$, and $\delta^{18}O$ and stratigraphic height. The $\delta^{238}U$ panel includes comparisons with estimated Ordovician seawater and modern carbonate and seawater reference values.

carbonate value, and the blue line representing the 0.15‰ offset between seawater and carbonate values (Chen et al., 2018).

Organic Carbon, Nitrogen, TOC, and TN

Total organic carbon values in 30 carbonate samples ranged from 0.013% to 0.998%, with an average of 0.22±0.29% (1σ) (Figure 9). There may be a slight increase upsection in the organic content of the samples. Carbon isotope values from organic carbon residue samples ranged from -26.73% to -29.31%, with an average of -28.48±0.87% (1σ). Samples lower in the stratigraphic column display $\delta^{13}C$ depletion and averages that align with other studies done on rocks from the Middle to Late Ordovician. %TOC values are consistent and stable, except for an outlier near 1 wt.% that may reflect localized organic enrichment or analytical variability. %TN also has outliers in the Edinburg Formation, however, it is consistent with related studies. The $\delta^{15}N$ panel shows values ranging from about -10‰ to +15‰, with stable values throughout the Edinburg. Little viable data was collected before the Edinburg; however, the few data points available show higher $\delta^{15}N$ values. All samples were analyzed for $\delta^{15}N$, however, samples with low peak height carry greater analytical uncertainty and were omitted.

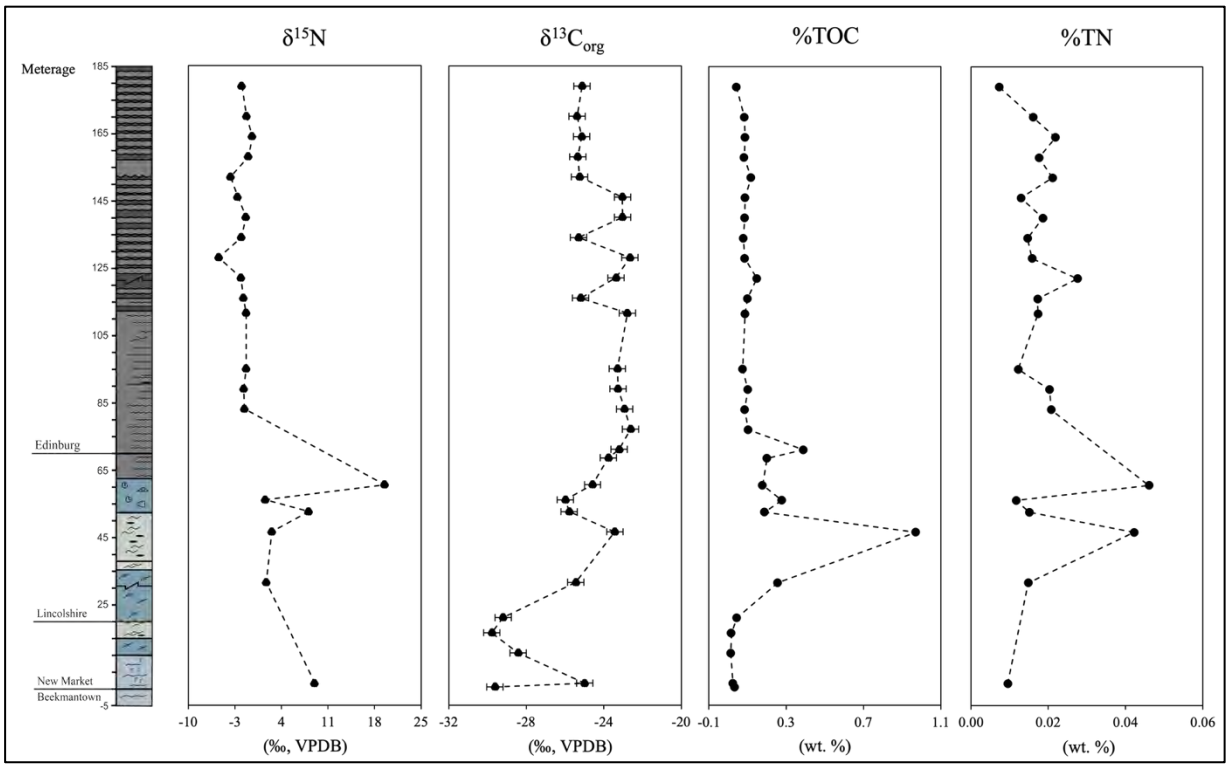

Figure 9. Chemostratigraphic plot showing the vertical distribution of $\delta^{13}C_{org}$, %TOC, %TN, $\delta^{15}N$ values with stratigraphic height across the Beekmantown, New Market, Lincolnshire, and Edinburg Formations. All data points include error bars (1σ), though in some cases the uncertainty is smaller than the symbol and thus not visible.

Standards, Uncertainties, and Precision

Analytical uncertainty for $\delta^{238}U$ was determined using two independent runs of each sample. External reproducibility was monitored through repeated analysis of the international uranium standard CRM-129a, which produced a median value of -1.72 ± 0.10‰ (2 SD). The known offset value for CRM-129a is -1.70‰. Individual sample uncertainties for $\delta^{238}U$ range from ±0.03‰ to ±0.09‰ (Appendix A-3). All $\delta^{13}C_{carb}$ and $\delta^{18}O$ values are reported relative to the Vienna Pee Dee Belemnite (VPDB) scale. VPDB represents the known $^{13}C/^{12}C$ ratio of the original Pee Dee Belemnite material from South Carolina. Although the physical standard no longer exists, its isotopic ratio is known. The internal carbonate standards used in this study are calibrated against VPDB, ensuring that measured $\delta^{13}C_{carb}$ and $\delta^{18}O$ values are directly comparable to published datasets. Two internal carbonate standards, JTB and MCC, were run repeatedly during $\delta^{13}C_{carb}$ and $\delta^{18}O$ analysis. The standard deviations from multiple runs of these standards were used to determine analytical precision for $\delta^{13}C_{carb}$ and $\delta^{18}O$. Across all samples, the standard deviations applied were: $\delta^{13}C$: 0.18‰ and $\delta^{18}O$: 0.16‰ (Appendix A-3). Urea standards were used for $\delta^{13}C_{org}$ and $\delta^{15}N$ analyses (Appendix A-3). These standard deviations were used as correction factors when calculating the final $\delta^{13}C_{org}$ and $\delta^{15}N$ values. The average $\delta^{13}C_{org}$ composition for 19 urea samples run during the analytical session was -39.75‰ (known value is -29.39‰) with a standard deviation of 0.42‰, and the abundance was 20.00 wt% (true value is 20 wt%) with a standard deviation of 0.23 wt%. The average $\delta^{15}N$ composition for the same 19 urea samples run during the analytical session was 1.59‰ (known value is -1.18‰) with a standard deviation of 0.15‰, and the abundance was 46.64 wt% (true value is 46 wt%)

with a standard deviation of 0.30 wt%. Blanks were measured across all analyses to determine and correct any background noise. Unfortunately, Pyrite analysis was not completed in time for this thesis but it remains a promising avenue for future work. Sulfur isotopes and trace metal associations in pyrite could provide complementary redox information to strengthen interpretations.

Discussion

Several key features across the stratigraphic successions provide essential context for the geochemical measurements. Evidence of karstification (including cave deposits) was observed within the Beekmantown dolomites, indicating exposure and erosion. This exposure was potentially the result of the plate being uplifted during an initial phase of continental collision. At Tumbling Run, the Knox unconformity was visible, showing an erosional contact between the dolomitic Beekmantown Group and the overlying limestone of the New Market Formation. In the New Market, bedding ranged from thin to thick, with the presence of fenestrae likely resulting from the replacement of evaporite minerals. The carbonates here were largely micritic and light grey in color, suggesting low organic carbon contents, which is consistent with the very low %TOC values. Moving into the Lincolnshire Formation, layers of thin ribbon-bedded carbonate with abundant black chert are much darker in color, suggesting higher organic carbon content, which is reflected in the %TOC increase relative to the underlying New Market Formation. Near the top of the Lincolnshire, there is an increase in shale content and siliciclastics, likely reflecting enhanced weathering inputs, possibly linked to the erosion of volcanic sources responsible for the volcanic ash. The Edinburgh Formation has abundant interbedded siliciclastic material and nodular limestone, which may indicate even greater weathering inputs. Overall, the succession displayed sedimentological features consistent with deepening waters and increasing erosion, potentially driven by tectonic activity associated with the Taconic Orogeny.

Uranium, Carbonate Carbon, Cerium, and Oxygen

The uranium concentrations in the samples (0.063-0.351 ppm) (Appendix A-3) are consistent with other measured Ordovician carbonates, which show overall low uranium concentrations. For example, Marenco et al. (2016) reported an average uranium concentration of 0.49 ppm (std. dev: 0.41) in the Pogonip Group carbonates from Utah (Lower-Middle Ordovician). Uranium is soluble in oxic conditions and precipitates under reducing conditions; therefore, low uranium content could suggest deposition under relatively anoxic bottom waters (Edwards, 2019). However, as Edwards (2019) also notes, the use of $\delta^{238}U$ is more diagnostic of redox than uranium concentration alone due to potential influences from microbial activity, carbonate mineralogy, and diagenesis. The $\delta^{238}U$ values from the Beekmantown, New Market, and Lincolnshire formations range from approximately -0.9‰ to -0.2‰. Modern shallow marine carbonates are typically 0.3‰ lighter than seawater due to early diagenetic reduction and incorporation of isotopically positive U species into carbonate minerals (Chen et al., 2018). All the seawater and carbonate $\delta^{238}U$ values are more negative than modern seawater and carbonate values, which is consistent with intervals of more widespread marine anoxia. There exists only one previous uranium isotope redox study for the GOBE (Rey et al., 2022), which revealed more negative $\delta^{238}U$ compositions in carbonates from Sweden in the interval before and at the onset of the GOBE (Figure 10). If true, these variations (tested in this comparative study) suggest that

uranium was removed in the preceding interval due to widespread anoxia and may thus explain the unusually low concentrations in the sample suite. The values align with data from this study, agreeing with the interpretation of anoxic waters, although this study displays more negative values. The remaining samples were prepared for analysis but could not be measured due to an unexpected instrument malfunction. The upper portion of the section could have shown an increasing trend indicative of oxic conditions, highlighting a valuable direction for future work.

The Ordovician $\delta^{18}O$ values in this study range from approximately -9‰ to -6‰ (VPDB), which is markedly lighter than modern marine carbonates at -1‰ to +1‰ (Carpenter & Lohmann, 1995; Douglas & Savin, 1971). The values are also broadly consistent with the global compilation of Veizer et al. (1999). In Veizer's dataset, Ordovician brachiopods typically plot between -6‰ and -3‰ while many Paleozoic carbonates exhibit even lighter values, often extending toward -8‰ or lower. The consistency of the values suggests good preservation through most of the section and is also consistent with data from Qing & Veizer (1994) and Diamond et al. (2024).

In contrast to the strongly altered $\delta^{18}O$ signal, $\delta^{13}C_{carb}$ values in this dataset remain stable, ranging from roughly -1‰ to +1‰. This narrow range is consistent with Veizer et al. (1999). The data trend directly correlates to the trends seen in Edwards & Saltzman (2016) (Figure 11). The stability of $\delta^{13}C_{carb}$ supports its utility for stratigraphic correlation among the New Market, Lincolnshire, and Edinburg Formations and indicates enhanced organic productivity and burial rates.

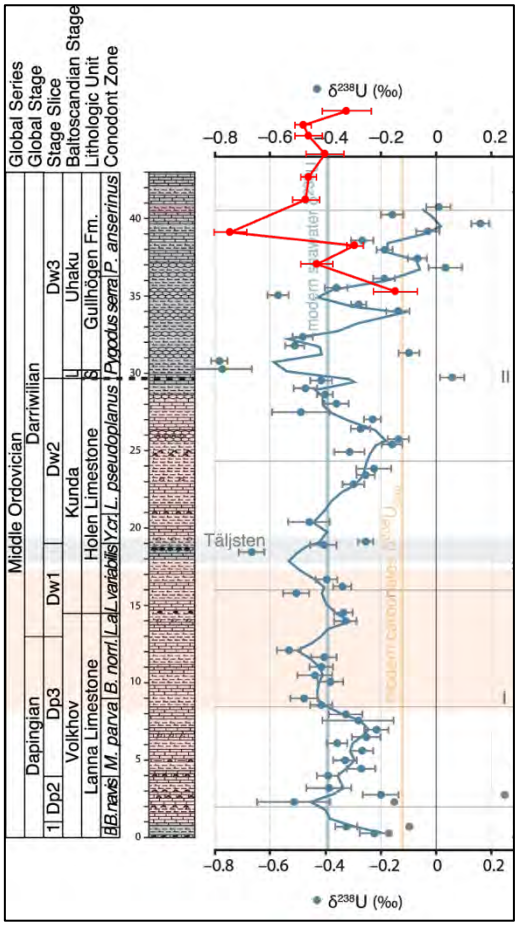

Figure 10. A plot of $\delta^{238}U$, from the only known study of uranium isotopes associated with the GOBE, shows low values before the peak of the event (displayed with yellow highlight). Uranium isotope values are more negative, indicating widespread anoxia before an increase in $\delta^{238}U$ and oxic conditions. (Rey et al., 2022). Data from this study is plotted in red and correlated using (Taylor et al., 2012).

Preliminary rare earth element data were obtained at the end of November for cerium anomaly analysis, including measurements of ^{139}La, ^{140}Ce, ^{141}Pr, and ^{143}Nd. Although efforts to correct and interpret these began, ultimately full analysis could not be completed. The raw signal intensities are provided in Appendix A-3 and have not been blank-subtracted or normalized to an internal standard. This dataset remains a promising opportunity for future work.

Organic Carbon, Nitrogen, TOC, and TN

The lower interval contains higher total organic carbon and more negative $\delta^{13}C_{org}$ values compared to overlying units. This shift could reflect differences in productivity, organic matter source, or redox conditions in the water column. The increased abundance of organic matter, combined with the isotopically depleted carbon, suggests enhanced preservation under more

reducing conditions. Facies evolution from shallow fenestral limestones to deeper ribbon cherts and then siliciclastics also indicates a changing depositional environment that may have influenced organic matter sources and preservation. Other Ordovician carbonate studies have found similar $\delta^{13}C_{org}$ values to those reported here. For example, an average of -29.51% (std. dev: 0.51%) in the Darriwilian-aged Fågelsång-3 core in Sweden was reported by Bergström et al. (2018). Negative $\delta^{13}C_{org}$ values primarily reflect biological fractionation during photosynthesis and subsequent microbial activity. The $\delta^{13}C_{org}$ values in this dataset are notably lower than those seen in the Clear Spring, MD section presented in Edwards & Saltzman (2016)

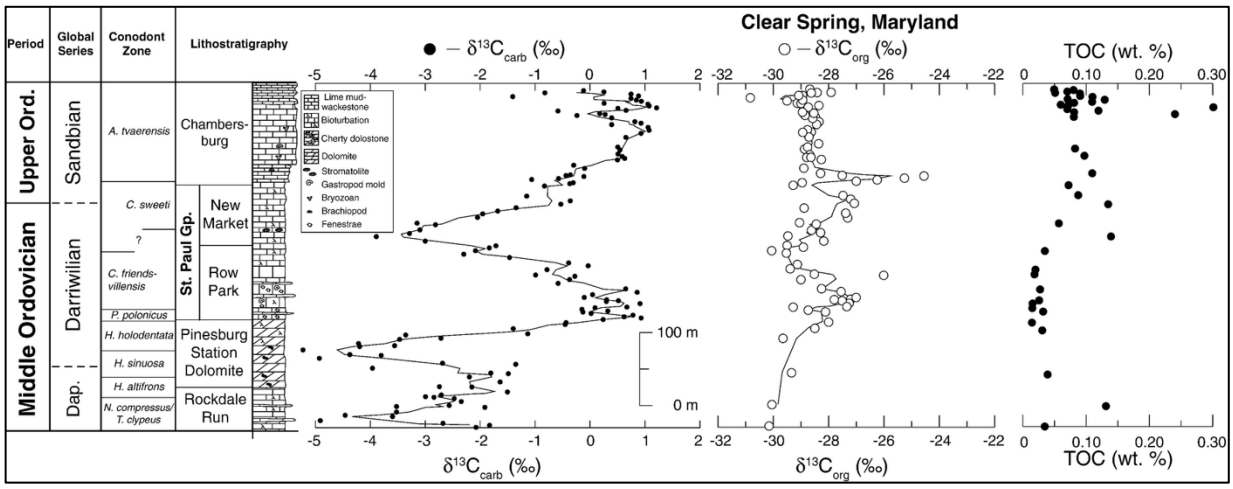

Figure 11. Carbon isotope data and total organic carbon from the Clear Spring section in Maryland, plotted alongside a lithostratigraphic column and biostratigraphy. The New Market under lithostratigraphy is the same formation as the New Market Formation from this study. Moving averages are shown for isotopic data. Modified from Edwards & Saltzman (2016).

(Figure 11). This discrepancy may reflect differences in methodology or diagenetic alteration. Despite the offset, the overall stratigraphic trend, including a general increase upsection, resembles the Clear Spring pattern.

A detailed inspection of peak heights revealed that several measurements fell below the threshold necessary for reliable isotope values. Carbon or nitrogen peak heights below approximately 3 nanoamps were considered inadequate and therefore rejected. These samples tend to produce unreliable $\delta^{13}C$ and $\delta^{15}N$ estimates. All samples flagged as problematic in the peak height table were removed from the final dataset (Appendix A-3). In addition, one sample around 39 meters showed both unusually low peak heights and anomalous isotope values, and because it was not successfully duplicated during the second run, it was excluded from all plots and interpretations. The earlier carbon-only run yielded values that were broadly similar in trend but exhibited a systematic offset relative to the C and N analyses for several samples, likely due to differences in dilution and gas handling conditions. For this reason, and to avoid mixing datasets generated under different instrumental conditions, all interpretations rely exclusively on the second analytical run.

Although the nitrogen dataset is limited due to low nitrogen abundance in many samples, the values that do meet quality standards exhibit a coherent pattern. The lower interval of the section contains the highest nitrogen abundances and shows enriched $\delta^{15}N$ values relative to the upper interval. This enrichment is consistent with denitrification, an anaerobic microbial process that preferentially removes isotopically light nitrogen from the water column. Residual nitrate becomes enriched in ^{15}N, and organic matter encompasses this heavy isotope signature. Therefore, the nitrogen isotopes suggest that the lower part of the succession experienced more

oxygen-limited water conditions during deposition. The values are slightly consistent with other Ordovician carbonate studies, such as, Yang et al. (2021) which produced $\delta^{15}N$ values ranging between 0.05‰ to 4.83‰. The outliers in the lower intervals are more enriched and interpretations for this enrichment in ongoing. Future studies could further analyze these discrepancies. Nitrogen was added to the dataset this semester as it is efficient to collect $\delta^{15}N$ data and total nitrogen (%TN) while analyzing for $\delta^{13}C$ and total organic carbon (%TOC), providing a more complete geochemical picture without needing separate preparation or instrumentation.

Taken together, the carbon and nitrogen data indicate a clear environmental transition within the stratigraphic succession. The lower interval is characterized by higher organic carbon content, higher nitrogen content, enriched $\delta^{15}N$ values, and more negative $\delta^{13}C_{org}$. These values support the interpretation that the lower interval was deposited under relatively more anoxic conditions than the upper interval. In contrast, the upper interval shows lower TOC, lower nitrogen content, and lower $\delta^{15}N$ values, consistent with deposition in more oxygenated water settings. This interpretation aligns with previously collected uranium isotope data from the same interval, which also suggest enhanced anoxia in the lower portion of the section.

Conclusions

The geochemical, sedimentological, and isotopic data from the Beekmantown, New Market, Lincolnshire, and Edinburg Formations provide a coherent picture of the Middle Ordovician oceans and allow a direct evaluation of the proposed link between marine oxygenation and the GOBE. The combined $\delta^{18}O$, $\delta^{238}U$, and $\delta^{13}C$ values, cerium anomalies, and organic geochemical proxies demonstrate that the lower and upper interval of the section was deposited under anoxic conditions, while the middle interval reflects oxygenated waters but is still depleted compared to modern oceans. Enriched $\delta^{15}N$ values and more negative $\delta^{13}C_{org}$ in the lower interval point to enhanced denitrification and organic matter preservation, consistent with reduced oxygen availability. These interpretations align with previously published studies that suggest intervals of widespread anoxia preceding or accompanying the onset of the GOBE. The carbonate $\delta^{238}U$ values are significantly more negative than modern seawater, indicating that seawater uranium was isotopically light, consistent with enhanced global removal of U under reducing conditions. These results are broadly comparable to the only other uranium isotope record across this time interval (Rey et al., 2022), reinforcing the conclusion that widespread marine anoxia was present during the early stages of biodiversification.

Taken together, these observations do not support the primary working hypothesis that the Middle Ordovician interval at Strasburg records a rise in oxygenation. Instead, the data aligns more closely with the secondary hypothesis: that Middle Ordovician oceans experienced intervals of decreased oxygenation, reflected in negative $\delta^{238}U$ values and redox-sensitive trace element patterns. The persistence of anoxic or oxygen-limited waters through the lower portion of the stratigraphic succession challenges the connection between a rise in atmospheric or oceanic oxygen and an increase in biodiversification.

Overall, the data indicates that the early Paleozoic oxygenation state was dynamic, with intervals of anoxia persisting even as biodiversification accelerated. This finding implies that biological innovation during the GOBE may have been influenced by factors other than an increase in oxygen, such as tectonic movement or increased weathering of silicates. Future work pairing a greater span of time intervals, locations, and redox proxies will help further paint how

landscapes evolved during this pivotal interval and what role they truly played in driving the Great Ordovician Biodiversification Event.

References

Bergmann, K. D., Macdonald, F. A., & Swanson-Hysell, N. L. (2025). The causes and consequences of Ordovician cooling. *Annual Review of Earth and Planetary Sciences*, *53*. https://doi.org/10.1146/annurev-earth-040523-114630

Bergström, S. M., Ahlberg, P., Maletz, J., Lundberg, F., & Joachimski, M. M. (2018). Darriwilian (Middle Ordovician) chemostratigraphy linked to graptolite, conodont and trilobite biostratigraphy in the Fågelsång-3 drill core, Scania, Sweden. *GFF*, *140*(3), 229–240. https://doi.org/10.1080/11035897.2018.1466833

Carpenter, S. J., & Lohmann, K. C. (1995). $\delta^{18}O$ and $\delta^{13}C$ values of modern brachiopod shells. *Geochimica et Cosmochimica Acta*, *59*(18), 3749–3764. https://doi.org/10.1016/0016-7037(95)00291-7

Chen, X., Romaniello, S. J., Herrmann, A. D., & Anbar, A. D. (2018). Diagenetic effects on uranium isotope fractionation in carbonate sediments from the Bahamas. *Geochimica et Cosmochimica Acta*, *237*, 294–311. https://doi.org/10.1016/j.gca.2018.06.026

Cui, H., Kaufman, A. J., Xiao, S., Zhu, M., Zhou, C., & Liu, X.-M. (2015). Redox architecture of an Ediacaran ocean margin: Integrated chemostratigraphic ($\delta^{13}C$–$\delta^{34}S$–$^{87}Sr/^{86}Sr$–Ce/Ce*) correlation of the Doushantuo Formation, South China. *Chemical Geology*, *405*, 48–62. https://doi.org/10.1016/j.chemgeo.2015.04.009

Dahl, T. W., Boyle, R., Canfield, D. E., Connelly, J. A., Gill, B. C., Lenton, T. M., & Bizzarro, M. (2014). Uranium isotopes distinguish two geochemically distinct stages during the later Cambrian SPICE event. *Earth and Planetary Science Letters*, *401*, 313–326. https://doi.org/10.1016/j.epsl.2014.05.043

Diamond, C. W., Saltzman, M. R., Lyons, T. W., & Edwards, C. T. (2024). Middle Ordovician paleoenvironmental evolution of the western Laurentian carbonate platform: Evidence for persistent oxygenation of the shallow ocean and implications for biodiversification. *Palaeogeography Palaeoclimatology Palaeoecology*, *655*, 112499. https://doi.org/10.1016/j.palaeo.2024.112499

Douglas, R. G. and Savin, S. M. (1971). Isotopic analysis of planktonic foraminifera from the Cenozoic of northwest Pacific, Leg 6. Initial Rep. Deep See Drill. Proj. 6, 1123-1127.

Edwards, C. T. (2019). Links between early Paleozoic oxygenation and the Great Ordovician Biodiversification Event (GOBE): A review. *Palaeoworld*, *28*(1-2), 37–50. https://doi.org/10.1016/j.palwor.2018.08.006

Edwards, C. T., & Saltzman, M. R. (2016). Paired carbon isotopic analysis of Ordovician bulk carbonate ($\delta^{13}C_{carb}$) and organic matter ($\delta^{13}C_{org}$) spanning the Great Ordovician Biodiversification Event. *Palaeogeography, Palaeoclimatology, Palaeoecology, 458*, 102–117. https://doi.org/10.1016/j.palaeo.2015.08.005

Epstein, S., Buchsbaum, R., Lowenstam, H., & Urey, H. C. (1951). Carbonate-water isotopic temperature scale. *Geological Society of America Bulletin*, *62*(4), 417. https://doi.org/10.1130/0016-7606(1951)62[417:cits]2.0.co;2

Gomes, M., Klatt, J., Dick, G., Grim, S., Rico, K., Medina, M., Ziebis, W., Kinsman-Costello, L., Sheldon, N., & Fike, D. (2021). Sedimentary pyrite sulfur isotope compositions preserve signatures of the surface microbial mat environment in sediments underlying low-oxygen cyanobacterial mats. *Geobiology*, *20*(1), 60–78. https://doi.org/10.1111/gbi.12466

Harper, D. A. T. (2023). Late Ordovician mass extinction: Earth, fire and ice. *National Science Review*, *11*(1). https://doi.org/10.1093/nsr/nwad319

Hayes, J. M. (1993). Factors controlling ^{13}C contents of sedimentary organic compounds: Principles and evidence. *Marine Geology*, *113*(1-2), 111–125. https://doi.org/10.1016/0025-3227(93)90153-m

Jones, D. S., Brothers, R. W., Crüger Ahm, A.-S., Slater, N., Higgins, J. A., & Fike, D. A. (2019). Sea level, carbonate mineralogy, and early diagenesis controlled $\delta^{13}C$ records in Upper Ordovician carbonates. *Geology*, *48*(2), 194–199. https://doi.org/10.1130/g46861.1

Kipp, M. A., Li, H., Ellwood, M. J., John, S. G., Middag, R., Adkins, J. F., & Tissot, F. L. H. (2022). ^{238}U, ^{235}U and ^{234}U in seawater and deep-sea corals: A high-precision reappraisal. *Geochimica et Cosmochimica Acta*, *336*, 231–248. https://doi.org/10.1016/j.gca.2022.09.018

Kolkas, M. M., & Friedman, G. M. (1998). Diagenetic history and geochemistry of the Beekmantown-Group dolomites (Sauk Sequence) of New York, USA. *Carbonates and Evaporites, 13*(1), 69–85. https://doi.org/10.1007/bf03175436

Kröger, B., & Lintulaakso, K. (2017). RNames, a stratigraphical database designed for the statistical analysis of fossil occurrences – the Ordovician diversification as a case study. *Palaeontologia Electronica*, *20*(1). https://doi.org/10.26879/729

Ku, T.-L., Mathieu, G. G., & Knauss, K. G. (1977). Uranium in open ocean: Concentration and isotopic composition. *Deep Sea Research*, *24*(11), 1005–1017. https://doi.org/10.1016/0146-6291(77)90571-9

Lawrence, M.G., Greig, A., Collerson, K.D., Kamber, B.S. (2006). Rare Earth Element and Yttrium Variability in South East Queensland Waterways. *Aquat Geochem 12*, 39–72. https://doi.org/10.1007/s10498-005-4471-8

Lenton, T. M., Crouch, M., Johnson, M., Pires, N., & Dolan, L. (2012). First plants cooled the Ordovician. *Nature Geoscience*, *5*(2), 86–89. https://doi.org/10.1038/ngeo1390

Li, N., Zhang, F., Gao, J., Cao, M., Wei, G.-Y., Wang, H., Zhang, Z., Cheng, M., Xiong, G., Zhou, J., Zhang, H., Peng, Y., Li, C., & Shen, S. (2022). Assessing bulk carbonates as archives for seawater sulfur isotopic composition using shallow water cores from the South China Sea. *Palaeogeography, Palaeoclimatology, Palaeoecology*, *598*, 111029. https://doi.org/10.1016/j.palaeo.2022.111029

Mackensen, A., & Schmiedl, G. (2019). Stable carbon isotopes in paleoceanography: Atmosphere, oceans, and sediments. *Earth-Science Reviews*, *197*, 102893. https://doi.org/10.1016/j.earscirev.2019.102893

Marcilly, C., Maffre, P., Le Hir, G., Pohl, A., Fluteau, F., Goddéris, Y., Donnadieu, Y., Heimdal, T., & Torsvik, T. H. (2022). Understanding the early Paleozoic carbon cycle balance and climate change from modelling. *Earth and Planetary Science Letters*, *594*, 117717. https://doi.org/10.1016/j.epsl.2022.117717

Marenco, P. J., Martin, K. R., Marenco, K. N., & Barber, D. C. (2016). Increasing global ocean oxygenation and the Ordovician Radiation: Insights from Th/U of carbonates from the Ordovician of western Utah. *Palaeogeography, Palaeoclimatology, Palaeoecology*, *458*, 77–84. https://doi.org/10.1016/j.palaeo.2016.05.014

Men, X., Mou, C., & Ge, X. (2022). Changes in palaeoclimate and palaeoenvironment in the Upper Yangtze area (South China) during the Ordovician–Silurian transition. *Scientific Reports*, *12*(1). https://doi.org/10.1038/s41598-022-17105-2

Miller, A. I., & Mao, S. (1995). Association of orogenic activity with the Ordovician Radiation of marine life. *Geology*, *23*(4), 305. https://doi.org/10.1130/00917613(1995)023%3C0305:aooawt%3E2.3.co;2

Nardin, E., Goddéris, Y., Donnadieu, Y., Le Hir, G., Blakey, R. C., Pucéat, E., & Aretz, M. (2011). Modeling the early Paleozoic long-term climatic trend. *Geological Society of America Bulletin*, *123*(5-6), 1181–1192. https://doi.org/10.1130/b30364.1

O'Neil, J.R (1977). Stable isotopes in mineralogy. *Phys Chem Minerals 2*, 105–123. https://doi-org.proxy-um.researchport.umd.edu/10.1007/BF00307527

Qing, H. and Veizer, J., (1994). Oxygen and carbon isotope composition of Ordovician brachiopods: Implications for coeval seawater. *Geochimica et Cosmochimica Acta*, 58: 1501-1509.

Read, J. & Repetski, J. (2012). Cambrian – lower Middle Ordovician passive carbonate margin, southern Appalachians, in J. R. Derby, R. D. Fritz, S. A. Longacre, W. A. Morgan, and C. A. Sternbach, eds., The great American carbonate bank: The geology and economic resources of the Cambrian – Ordovician Sauk megasequence of Laurentia: AAPG Memoir 98, p. 357 – 382.

Rey, A. D., Rasmussen, C., Calner, M., Wu, R., Asael, D., & Dahl, T. W. (2022). Stable ocean redox during the main phase of the Great Ordovician Biodiversification Event. *Communications Earth & Environment*, *3*(1). https://doi.org/10.1038/s43247-022-00548-w

Romaniello, S. J., Herrmann, A. D., & Anbar, A. D. (2013). Uranium concentrations and 238U/235U isotope ratios in modern carbonates from the Bahamas: Assessing a novel paleoredox proxy. *Chemical Geology*, *362*, 305–316. https://doi.org/10.1016/j.chemgeo.2013.10.002

Scotese, C. R. (2023). Ordovician plate tectonic and palaeogeographical maps. Geological Society, London, Special Publications, 532(1), 91–109. https://doi.org/10.1144/sp532-2022-311

Servais, T., & Harper, D. A. T. (2018). The Great Ordovician Biodiversification Event (GOBE): Definition, concept and duration. *Lethaia*, *51*(2), 151–164. https://doi.org/10.1111/let.12259

Servais, T., Owen, A. W., Harper, D. A. T., Kröger, B., & Munnecke, A. (2010). The Great Ordovician Biodiversification Event (GOBE): The palaeoecological dimension. *Palaeogeography, Palaeoclimatology, Palaeoecology*, *294*(3-4), 99–119. https://doi.org/10.1016/j.palaeo.2010.05.031

Sharp, Zachary. (2007). Principles of Stable Isotope Geochemistry. *The University of New Mexico*. https://doi.org/10.25844/h9q1-0p82

Sheehan, P. M. (2001). The Late Ordovician mass extinction. *Annual Review of Earth and Planetary Sciences*, *29*(1), 331–364. https://doi.org/10.1146/annurev.earth.29.1.331

Sperling, E. A., Frieder, C. A., Raman, A. V., Girguis, P. R., Levin, L. A., & Knoll, A. H. (2013). Oxygen, ecology, and the Cambrian radiation of animals. *Proceedings of the National Academy of Sciences*, *110*(33), 13446–13451. https://doi.org/10.1073/pnas.1312778110

Staal, V., & Hatcher, R. D. (2010). Global setting of Ordovician orogenesis. *Geological Society of America EBooks*. https://doi.org/10.1130/2010.2466(01)

Steemans, P., Herisse, A. L., Melvin, J., Miller, M. A., Paris, F., Verniers, J., & Wellman, C. H. (2009). Origin and radiation of the earliest vascular land plants. *Science*, *324*(5925), 353–353. https://doi.org/10.1126/science.1169659

Stillman, C. J. (1984). Ordovician volcanicity, in Bruton, D. L, ed., Aspects of the Ordovician system: Oslo, Norway, Universitetsforlaget, p. 183–194.

Swart, P. K. (2015). The geochemistry of carbonate diagenesis: The past, present and future. *Sedimentology*, *62*(5), 1233–1304. https://doi.org/10.1111/sed.12205

Taylor, J. F., Repetski, J. E., Loch, J. D., & Leslie, S. A. (2012). Biostratigraphy and chronostratigraphy of the Cambrian – Ordovician great American carbonate bank, in J. R. Derby, R. D. Fritz, S. A. Longacre, W. A. Morgan, and C. A. Sternbach, eds., The great American carbonate bank: The geology and economic resources of the Cambrian – Ordovician Sauk Megasequence of Laurentia: AAPG Memoir 98, p. 15 – 35. https://doi.org/10.1306/13331488m983497

Tazoe, H., Obata, H., Amakawa, H., Nozaki, Y., & Gamo, T. (2007). Precise determination of the cerium isotopic compositions of surface seawater in the Northwest Pacific Ocean and Tokyo Bay. *Marine Chemistry*, *103*(1-2), 1–14. https://doi.org/10.1016/j.marchem.2006.05.008

Tissot, F., & Dauphas, N. (2015). Uranium isotopic compositions of the crust and ocean: Age corrections, U budget and global extent of modern anoxia. *Geochimica et Cosmochimica Acta*, *167*, 113–143. https://doi.org/10.1016/j.gca.2015.06.034

Torsvik, T. H., & Cocks, L. R. M. (2017). Earth history and palaeogeography. *Cambridge University Press & Assessment.*

Tostevin, R., Shields, G. A., Tarbuck, G. M., He, T., Clarkson, M. O., & Wood, R. A. (2016). Effective use of cerium anomalies as a redox proxy in carbonate-dominated marine settings. *Chemical Geology*, *438*, 146–162. https://doi.org/10.1016/j.chemgeo.2016.06.027

Veizer, J., Ala, D., Azmy, K., Bruckschen, P., Buhl, D., Bruhn, F., Carden, G. A. F., Diener, A., Ebneth, S., Godderis, Y., Jasper, T., Korte, C., Pawellek, F., Podlaha, O. G., & Strauss, H. (1999). $^{87}Sr/^{86}Sr$, $\delta^{13}C$ and $\delta^{18}O$ evolution of Phanerozoic seawater. *Chemical Geology*, *161*(1-3), 59–88. https://doi.org/10.1016/s0009-2541(99)00081-9

Webby, B. D., Percival, I. G., Paris, F., & Droser, M. L. (2004). *The great Ordovician biodiversification event*. Columbia University Press.

Wellman, C. H., & Gray, J. (2000). The microfossil record of early land plants. *Philosophical Transactions of the Royal Society of London.* Series B: Biological Sciences, *355*(1398), 717–732. https://doi.org/10.1098/rstb.2000.0612

Yang, S., Hu, W., Wang, X., & Fan, J. (2021). Nitrogen isotope evidence for a redox-stratified ocean and eustasy-driven environmental evolution during the Ordovician-Silurian transition. Global and Planetary Change, 207, 103682. https://doi.org/10.1016/j.gloplacha.2021.103682

Acknowledgements

I would like to extend my gratitude and thanks to Dr. Alan Jay Kaufman for advising this project and for being patient with the many questions and tardy mornings. I would not be as confident as I am in this project without his dedication. I would also like to thank Dr. Philip Piccoli for guidance in the difficult navigation of senior thesis and the laughs along the way, as well as Matthew Pedersen and Tian Gan for providing lab support and quick answers to the many late-night emails full of repeating questions and Geoffrey Gilleaudeau and Madison Thompson for lab support at GMU. Lastly, a special thanks to Donovan Cunion and Sami Tiobero for the many caffeine-fueled late-night writing sessions that I will miss dearly, and Donna and Scott Henderson for the lifelong support and guidance.

Honor Code

I pledge on my honor that I have not given or received any unauthorized assistance or plagiarized on this assignment.

Appendix

A-1: Maps

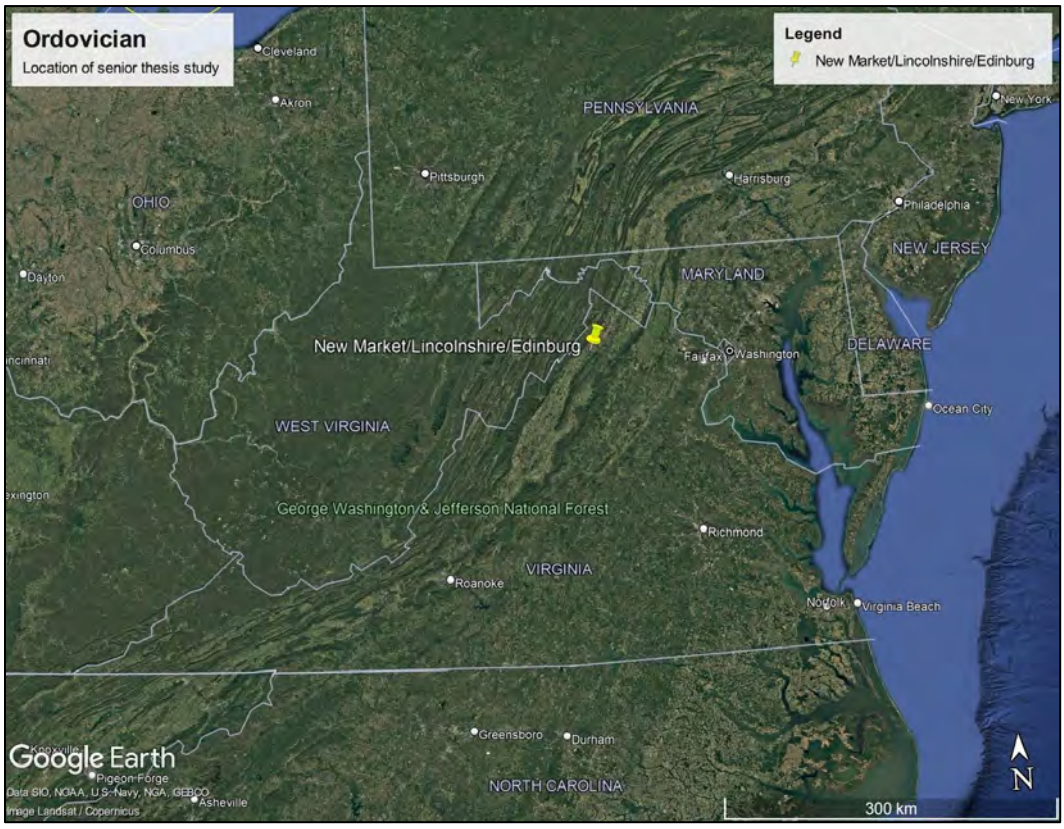

Figure 12. A map of Maryland and Virgina with the New Market, Lincolnshire, and Edinburg Formations Pinpointed.

A-2: Methods

Sulfur, Nitrogen, and Organic Carbon Isotope Preparation

Powders intended for C, N, and S analysis were prepared following the carbonate acidification protocol in the Gilleaudeau Lab. Approximately 1.5 g of homogenized carbonate powder was transferred into pre-weighed, 50 mL acid-leached centrifuge tubes. A disposable plastic pipette was used to slowly add 20 mL of 1 M trace-metal-grade HNO_3, then 5 mL of concentrated trace-metal-grade HNO_3, and finally 15 mL of 1 M trace-metal-grade HNO_3. The centrifuge tubes were then vortexed to thoroughly mix the powder and solution, which were allowed to react overnight. The following day, the tubes were centrifuged at 5,000 rpm for ten minutes, and the solution was decanted into a fresh 50 mL centrifuge tube, which was used for uranium isotope analysis. After the solution was decanted, an insoluble residue was left at the bottom of the tube, which was used for organic carbon and pyrite sulfur isotope analyses. The insoluble residue was rinsed with Milli-Q water and dried in an oven at 60 ºC. The dried samples were weighed and used to calculate the percent carbonate of the powders. The dried residue was used for C, N, TOC, and S isotope analysis.

Uranium Digestion and Column Chemistry

Supernatants designated for U isotope measurements were transferred into pre-cleaned Teflon beakers and progressively dried at 180 °C until only a small bead of liquid or slurry remained. Uranium concentrations from ICP-MS calibration were used to calculate the necessary volume of double spike (0.8 mL of ^{233}U-^{236}U per 500 ng U), which was then added to each beaker (Appendix, A-3). To calculate uranium concentrations, a linear trendline was generated, and the equation of the slope of the line was calculated (Figure 13). The amount of U in the rock was calculated using the following equation:

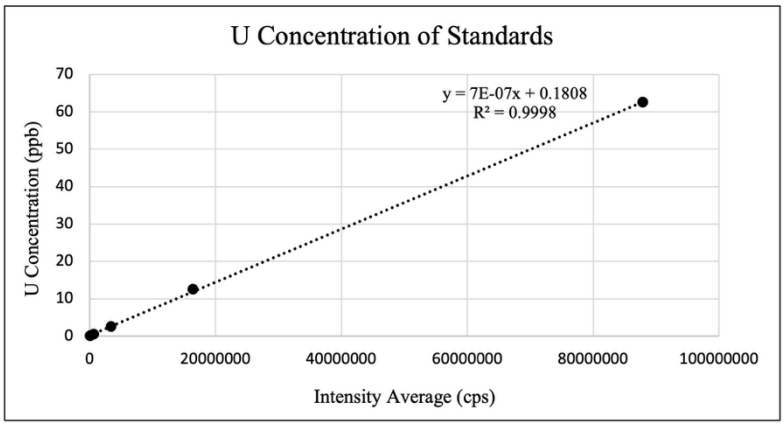

Figure 13. Calibration curve for U concentrations on the Element 2 ICP-MS during the June session. The positive linear trend between counts per second and concentration confirms instrument calibration accuracy, with the slope and R^2 value indicating excellent consistency across the standard range.

$$Rock\ U\ (ppm)\ = \left(\frac{\frac{final\ mL\ weight}{aliquot\ mL\ weight} * \frac{mL\ dissolved}{powder\ weight}}{1000} \right) * U_{concentration}$$

Samples were again dried and subsequently digested in 6 mL of reverse aqua regia (4.5 mL HNO_3 + 1.5 mL HCl), capped, and heated overnight. If insoluble material remained, additional reverse-aqua-regia digestions were performed.

After complete dissolution, the samples were dried partially and digested sequentially in HNO_3 + H_2O_2, pure HNO_3, and finally converted into 10 mL of 3 M HNO_3 to prepare for column chromatography. These digestion and dry-down cycles were monitored closely to avoid over-drying, which could prevent redissolution.

Purification of uranium from matrix elements followed the UTEVA resin protocol. Columns were conditioned with 3 M HNO_3, and the full 3 M HNO_3 sample solution was loaded to allow U and Th to adsorb to the resin. Matrix elements were removed using multiple 3 M HNO_3 washes. The resin was then converted to chloride form using 10 M HCl, and thorium was removed with repeated rinses of 5 M HCl containing 0.05 M oxalic acid. Uranium was subsequently eluted using ten 1 mL aliquots of 0.05 M HCl.

Post-UTEVA column, the samples were evaporated to dryness at 180° C, leaving a small white U residue adhered to the beaker walls. To prevent sample loss due to static, dry beakers were never left uncapped on the hot plate. The dried residue was digested to remove any remaining organics from the resin by adding 2 mL of concentrated trace-metal-grade HNO_3 and 0.2 mL of H_2O_2. Beakers were capped immediately after reagent addition, as the H_2O_2 caused vigorous bubbling, and were heated overnight at 180 °C. After cooling, the beakers were uncapped, and the solution was dried down again. The digestion step was repeated once more, followed by another overnight heating at 180 °C. Once cooled, the solution underwent one final preparation step in which 1 mL of 6 M trace-metal-grade HNO_3 was added. The beakers were capped and returned to 180 °C overnight. This final solution was used for loading onto the second column.

DGA resin columns were prepared by adding 1 mL of unbranched Eichrom DGA resin as a slurry in MQ water. Columns were cleaned and conditioned sequentially with ten 1 mL aliquots of 1 M HF (to clean the resin), ten 1 mL aliquots of 0.05 M HCl (to remove residual U), and ten 1 mL aliquots of 6 M HNO_3 (to prepare the resin for sample loading). Samples were then loaded onto the DGA columns in 6 M HNO_3. Following sample loading, the columns were rinsed with ten 1 mL aliquots of 6 M HNO_3 to remove Na and trace Fe. Clean, labeled sample beakers were placed beneath each column, and U was eluted using ten 1 mL aliquots of 0.05 M HCl. The combined eluate was dried down completely on a hot plate at 180 °C. As in previous steps, the small U residue occasionally formed a visible white dot, but its absence did not indicate sample loss. Beakers were handled carefully to avoid static-related U loss.

After cooling, the final solution was diluted in 2% HNO_3 to achieve a target concentration of 50 ppb U, based on results from prior ICP-MS screening of each sample. Beakers were capped and heated overnight at 180 °C to ensure complete dissolution and homogenization. Once cooled, the solutions were transferred into clean, labeled 15 mL metal-free centrifuge tubes. These prepared solutions were then submitted to the Neptune ICP-MS for U isotope analysis.

A-3: Isotope Data

Sample	Meterage	Formation	% Residue	% Carbonate	%TIC	%C	%TOC	%Total Carbon	%N	%TN
BGH_25_-0.5	-0.5	Beekmantown	1.171	98.83	11.86					
BGH_25_0.4	0.4	New Market	3.099	96.90	11.63	1.105	0.03424	11.66		
YDA_ST_1.5	1.5	New Market	2.892	97.11	11.65	0.8592	0.02484	11.68	0.3297	0.009534
YDA_ST_10.5	10.5	New Market	0.8264	99.17	11.90	1.619	0.01338	11.91		
YDA_ST_16.5	16.5	New Market	0.7921	99.21	11.90	2.050	0.01624	11.92		
YDA_ST_21	21	Lincolnshire	0.2513	99.75	11.97	17.78	0.04468	12.01		
YDA_ST_31.5	31.5	Lincolnshire	3.716	96.28	11.55	6.917	0.2570	11.81	0.3987	0.01481
YDA_ST_39	39	Lincolnshire	0.7243	99.28	11.91					
YDA_ST_46.5	46.5	Lincolnshire	2.489	97.51	11.70	38.98	0.9701	12.67	1.695	0.04217
YDA_ST_52.5	52.5	Lincolnshire	5.667	94.33	11.32	3.306	0.1874	11.51	0.2660	0.01508
YDA_ST_56	56	Lincolnshire	4.038	95.96	11.52	6.883	0.2780	11.79	0.2897	0.01170
YDA_ST_60.5	60.5	Lincolnshire	5.577	94.42	11.33	3.190	0.1779	11.51	0.8255	0.04604
BGH_25_68.5	68.5	Lincolnshire	12.64	87.36	10.48	1.582	0.2001	10.68		
YDA_ST_71	71	Lincolnshire	21.87	78.13	9.375	1.775	0.3882	9.763		
BGH_25_77	77	Edinburg	14.38	85.62	10.27	0.7173	0.1031	10.38		
BGH_25_83	83	Edinburg	12.51	87.49	10.50	0.6841	0.08561	10.58	0.1659	0.02077
BGH_25_89	89	Edinburg	13.80	86.20	10.34	0.7366	0.1017	10.45	0.1474	0.02034
BGH_25_95	95	Edinburg	8.607	91.39	10.97	0.8610	0.07410	11.04	0.1416	0.01219
BGH_25_111.5	111.5	Edinburg	13.09	86.91	10.43	0.6622	0.08667	10.52	0.1323	0.01731
BGH_25_116	116	Edinburg	11.17	88.83	10.66	0.8933	0.09981	10.76	0.1544	0.01725
BGH_25_122	122	Edinburg	17.07	82.93	9.952	0.8709	0.1486	10.10	0.1615	0.02757
BGH_25_128	128	Edinburg	12.76	87.24	10.47	0.6716	0.08568	10.55	0.1240	0.01582
BGH_25_134	134	Edinburg	9.491	90.51	10.86	0.8277	0.07856	10.94	0.1543	0.01464
BGH_25_140	140	Edinburg	11.14	88.86	10.66	0.7679	0.08552	10.75	0.1671	0.01861
BGH_25_146	146	Edinburg	8.368	91.63	11.00	1.051	0.08796	11.08	0.1549	0.01296
BGH_25_152	152	Edinburg	11.73	88.27	10.59	1.008	0.1182	10.71	0.1797	0.02108
BGH_25_158	158	Edinburg	9.977	90.02	10.80	0.8323	0.08304	10.89	0.1764	0.01760
BGH_25_164	164	Edinburg	12.45	87.55	10.51	0.7043	0.08768	10.59	0.1756	0.02186
BGH_25_170	170	Edinburg	10.83	89.17	10.70	0.7691	0.08332	10.78	0.1484	0.01607
BGH_25_179	179	Edinburg	4.517	95.48	11.46	0.9442	0.04265	11.50	0.1620	0.007319

Table 1. Shown are calculations on raw carbon data from the Multiflow Isoprime gas source mass spectrometer done in the spring. Weight of tube, sample, and after acid were all manual measurements. Weight of the residue was calculated as weight after acid subtracted from the weight of tube. Percent residue was calculated as (weight of the residue divided by weight of the sample) multiplied by 100. Percent total inorganic carbon was calculated as percent carbonate multiplied by 0.12 (the weight percent of carbon in carbonates). Percent carbon, nitrogen, and ^{13}C was raw data provided. Percent total organic carbon and percent total nitrogen was calculated as percent carbon/nitrogen multiplied by (percent residue over 100). Total carbon was calculated as total organic carbon plus total inorganic carbon.

Sample	Meterage	Formation	U Conc. (ppm)	Initial Powder wt. (g)	Powder Dissolved in (mL)	Aliquot of Solution (mL)	Acid	Final Solution Volume (mL)	Dilution Factor to Rock (ppb)	Dilution Factor to Rock (ppm)	U in Rock (ppm)	U (ng)	mL to Dry Down	Target ng	mL Spike to Add
BGH_25_-0.5	-0.5	Beekmantown	1.211	1.496	40.00	0.2000	9.860	10.06	1345	1.345	1.629	2437	4.925	300.0	0.4800
BGH_25_0.4	0.4	New Market	0.7257	1.513	40.00	0.2000	9.871	10.07	1331	1.331	0.9662	1462	8.209	300.0	0.4800
YDA_ST_1.5	1.5	New Market	0.9740	1.553	40.00	0.2181	9.743	9.961	1176	1.176	1.146	1779	6.744	300.0	0.4800
YDA_ST_10.5	10.5	New Market	0.6335	1.513	40.00	0.2200	10.05	10.27	1235	1.235	0.7824	1183	10.14	300.0	0.4800
YDA_ST_16.5	16.5	New Market	0.8165	1.578	40.00	0.2188	9.873	10.09	1169	1.169	0.9546	1506	7.966	300.0	0.4800
YDA_ST_21	21	Lincolnshire	0.5164	1.552	40.00	0.2134	9.733	9.947	1201	1.201	0.6203	962.8	12.46	300.0	0.4800
YDA_ST_31.5	31.5	Lincolnshire	0.5079	1.550	40.00	0.2081	10.01	10.22	1268	1.268	0.6439	998.1	12.02	300.0	0.4800
YDA_ST_39	39	Lincolnshire	0.5196	1.505	40.00	0.2180	9.921	10.14	1236	1.236	0.6423	966.6	12.41	300.0	0.4800
YDA_ST_46.5	46.5	Lincolnshire	0.6473	1.539	40.00	0.2203	9.757	9.977	1177	1.177	0.7619	1173	10.23	300.0	0.4800
YDA_ST_52.5	52.5	Lincolnshire	0.5242	1.576	40.00	0.2189	9.778	9.997	1159	1.159	0.6077	957.6	12.53	300.0	0.4800
YDA_ST_56	56	Lincolnshire	0.5316	1.530	40.00	0.2188	9.815	10.03	1199	1.199	0.6373	975.2	12.30	300.0	0.4800
YDA_ST_60.5	60.5	Lincolnshire	0.4865	1.519	40.00	0.2158	9.828	10.04	1226	1.226	0.5963	905.7	13.25	300.0	0.4800
BGH_25_68.5	68.5	Lincolnshire	0.2904	1.555	40.00	0.2000	9.880	10.08	1297	1.297	0.3767	585.5	20.49	300.0	0.4800
YDA_ST_71	71	Lincolnshire	0.4482	1.495	40.00	0.2000	9.921	10.12	1354	1.354	0.6067	907.3	13.23	300.0	0.4800
BGH_25_77	77	Edinburg	0.3118	1.545	40.00	0.2000	9.880	10.08	1305	1.305	0.5847	903.6	13.28	300.0	0.4800
BGH_25_83	83	Edinburg	0.2653	1.532	40.00	0.2000	9.880	10.08	1316	1.316	0.4103	628.5	19.09	300.0	0.4800
BGH_25_89	89	Edinburg	0.3124	1.578	40.00	0.2000	9.880	10.08	1278	1.278	0.3390	534.8	22.44	300.0	0.4800
BGH_25_95	95	Edinburg	0.3089	1.494	40.00	0.2000	9.880	10.08	1350	1.350	0.4217	629.9	19.05	300.0	0.4800
BGH_25_111.5	111.5	Edinburg	0.2858	1.494	40.00	0.2000	9.880	10.08	1350	1.350	0.4169	622.7	19.27	300.0	0.4800
BGH_25_116	116	Edinburg	0.3353	1.529	40.00	0.2000	9.880	10.08	1319	1.319	0.3769	576.2	20.82	300.0	0.4800
BGH_25_122	122	Edinburg	0.4034	1.515	40.00	0.2000	9.880	10.08	1331	1.331	0.4461	675.9	17.75	300.0	0.4800
BGH_25_128	128	Edinburg	0.2824	1.492	40.00	0.2000	9.880	10.08	1352	1.352	0.5452	813.2	14.76	300.0	0.4800
BGH_25_134	134	Edinburg	0.2616	1.522	40.00	0.2000	9.880	10.08	1325	1.325	0.3741	569.3	21.08	300.0	0.4800
BGH_25_140	140	Edinburg	0.5250	1.565	40.00	0.2000	9.880	10.08	1288	1.288	0.3371	527.5	22.75	300.0	0.4800
BGH_25_146	146	Edinburg	0.4566	1.505	40.00	0.2000	9.880	10.08	1340	1.340	0.7035	1058	11.34	300.0	0.4800
BGH_25_152	152	Edinburg	0.5419	1.503	40.00	0.2000	9.880	10.08	1341	1.341	0.6125	920.5	13.04	300.0	0.4800
BGH_25_158	158	Edinburg	0.5082	1.545	40.00	0.2000	9.880	10.08	1305	1.305	0.7070	1092	10.98	300.0	0.4800
BGH_25_164	164	Edinburg	0.4850	1.496	40.00	0.2000	9.880	10.08	1348	1.348	0.6851	1025	11.71	300.0	0.4800
BGH_25_170	170	Edinburg	0.3601	1.587	40.00	0.2000	9.880	10.08	1271	1.271	0.6163	977.7	12.27	300.0	0.4800
BGH_25_179	179	Edinburg	0.1881	1.569	40.00	0.2000	9.880	10.08	1285	1.285	0.4626	725.9	16.53	300.0	0.4800

Table 2. Shown are calculations on raw uranium data from the Element 2 inductively coupled plasma mass spectrometer to achieve the correct amount of sample to dry down. Initial powder weight, powder dissolved, aliquot of solution, acid, and solution volume were all manual measurements. The dilution factor was calculated using (final solution divided by an aliquot of the solution) multiplied by (powder dissolved divided by initial powder weight). The values were converted to ppm. The uranium in the sample was calculated as the uranium concentration multiplied by the dilution factor in ppm. Uranium mass in ng was calculated as initial powder weight multiplied by uranium in rock ppm multiplied by 1000. The amount to dry down in mL was calculated as (target mass over mass) multiplied by powder dissolved.

First Run

Sample	Meterage	CO_2 Height (nA)	N_2 Height (nA)	^{13}C Raw	^{13}C Corr	%C Raw	%C Corr	^{15}N Raw	^{15}N Corr	%N Raw	%N Corr
urea R1		4.335	15.97	-40.33		20.10		1.351		46.90	
urea R2		4.573	17.11	-39.91		19.69		1.537		46.32	
urea R3		4.910	18.39	-39.94		19.76		1.456		46.45	
urea R4		4.660	17.45	-40.03		19.94		1.460		46.91	
urea R5		4.880	18.25	-40.00		19.92		1.459		46.76	
BH 94_5		14.27	3.441	-33.66	-23.05	0.8610	0.8610	-0.9230	-1.223	0.1416	0.1416
BGH_25_134	134	12.78	3.535	-35.66	-25.05	0.8277	0.8277	-1.668	-1.968	0.1543	0.1543
BGH_25_89	89	11.88	3.460	-33.63	-23.02	0.7366	0.7366	-1.304	-1.604	0.1474	0.1474
BGH_25_140	140	12.31	4.013	-33.40	-22.79	0.7679	0.7679	-0.9505	-1.250	0.1671	0.1671
BGH_25_122	122	14.32	3.959	-33.73	-23.12	0.8709	0.8709	-1.699	-1.999	0.1615	0.1615
BGH_25_146	146	15.74	3.567	-33.40	-22.79	1.051	1.051	-2.215	-2.515	0.1549	0.1549
BGH_25_152	152	15.83	4.319	-35.61	-25.00	1.008	1.008	-3.287	-3.587	0.1797	0.1797
BGH_25_77	77	11.35	2.586	-32.98	-22.37	0.7173	0.7173	-3.065	-3.365	0.1153	0.1153
BGH_25_83	83	10.83	3.968	-33.29	-22.68	0.6841	0.6841	-1.199	-1.499	0.1659	0.1659
BGH_25_68_5	68.5	19.94	2.017	-112.5	-101.9	1.475	1.475	-6.139	-6.439	0.0951	0.0951
blank 5		0.04152	0.2023	-32.99				-41.15			
		0.001989		126.0							
urea R6		4.622	17.05	-40.65		20.11		1.301		46.63	
urea R7		5.192	19.35	-39.49		20.20		1.388		47.00	
urea R8		4.913	17.92	-39.92		20.29		1.604		46.80	
BGH_25_68_5 rep	68.5	12.46	1.053	-34.12	-23.51	1.582	1.582	-6.306	-6.606	0.1139	0.1139
BGH_YDA_ST_71_oldertube	71	14.41	1.594	-33.46	-22.85	1.794	1.794	7.474	7.174	0.1541	0.1541
BGH_YDA_ST_52_5	52.5	9.188	0.9418	-36.14	-25.53	3.306	3.306	7.619	7.319	0.3097	0.3097
BGH_YDA_ST_56	56	10.61	0.6682	-36.34	-25.73	6.883	6.883	-5.654	-5.954	0.4477	0.4477
BGH_YDA_ST_60_5	60.5	6.962	2.371	-37.07	-26.46	3.063	3.063	16.99	16.69	0.7777	0.7777
BGH_YDA_ST_46_5	46.5	15.99	1.033	-33.80	-23.19	38.98	38.98	-1.156	-1.456	2.207	2.2074
BGH_25_116	116	14.67	3.793	-35.55	-24.94	0.8933	0.8933	-1.344	-1.644	0.1544	0.1544
BGH_25_179	179	14.88	3.877	-35.49	-24.88	0.9442	0.9442	-1.587	-1.887	0.1620	0.1620
BGH_25_111_5	111.5	10.16	2.954	-33.15	-22.54	0.6622	0.6622	-0.9320	-1.232	0.1323	0.1323
BGH_25_170	170	12.69	3.687	-35.74	-25.13	0.7691	0.7691	-0.8835	-1.184	0.1484	0.1484
blank 6		0.06073	0.1923	-24.25				-30.01			
urea R9		5.050	18.77	-39.64		19.96		1.555		46.34	
urea R10		4.889	18.13	-40.09		20.03		1.673		46.27	

Table 3. First run of $\delta^{13}C$ and $\delta^{15}N$ analysis completed during Fall 2025. Values highlighted indicate unreliable isotope results due to low peak heights. $\delta^{13}C$ and $\delta^{15}N$ values were corrected using an offset determined from urea standards.

Second Run

Sample	Meterage	CO_2 Height (nA)	N_2 Height (nA)	^{13}C Raw	^{13}C Corr	%C Raw	%C Corr	^{15}N Raw	^{15}N Corr	%N Raw	%N Corr
urea R1		4.352	16.51	-39.88		20.00		1.682		47.06	
urea R2		4.691	17.78	-39.29		19.74		1.720		46.37	
urea R3		5.017	18.99	-39.06		19.94		1.698		46.74	
urea R4		4.658	17.59	-39.71		20.00		1.658		46.97	
urea R5		4.883	18.41	-39.50		20.02		1.685		46.92	
BGH_25_164	164	11.34	4.336	-35.50	-25.42	0.7043	0.7043	-0.02643	-0.4564	0.1756	0.1756
BGH_25_158	158	13.08	4.286	-35.71	-25.63	0.8323	0.8323	-0.5949	-1.025	0.1764	0.1764
BGH_25_128	128	10.32	2.892	-36.24	-26.16	0.6481	0.6481	-2.563	-2.993	0.1259	0.1259
BGH_25_-0_5	-0.5	1.393	0.2439	-36.22	-26.14	3.369	3.369	-18.92	-19.35	0.8736	0.8736
BGH_25_0_4	0.4	17.52	2.554	-39.98	-29.90	1.105	1.105	-5.325	-5.755	0.1067	0.1067
YDA_ST_71_newertube	71	14.23	1.062	-33.57	-23.49	1.775	1.775	-16.90	-17.33	0.1140	0.1140
YDA_ST_39	39	2.225	0.3315	-45.24	-35.16	4.294	4.294	-18.78	-19.21	0.9239	0.9239
YDA_ST_1_5	1.5	12.94	7.947	-35.35	-25.27	0.8592	0.8592	9.374	8.944	0.3297	0.3297
YDA_ST_10_5	10.5	4.814	2.118	-38.78	-28.70	1.619	1.619	6.706	6.276	0.5273	0.5273
YDA_ST_46_5 rep	46.5		3.247					2.982	2.552	1.695	1.695
blank 5		0.03346	0.2148	-39.37				-32.90			
urea R7		4.978	18.99	-39.54		19.71		1.683		46.46	
urea R8		4.616	17.30	-39.87		19.73		1.686		45.98	
YDA_ST_60_5 rep	60.5	12.47	4.979	-34.94	-24.86	3.190	3.190	19.91	19.48	0.8255	0.8255
YDA_ST_31_5	31.5	19.91	1.633	-98.79	-88.71	6.769	6.769	0.9664	0.5364	0.3866	0.3866
YDA_ST_16_5	16.5	4.629	1.518	-40.14	-30.06	2.050	2.050	1.580	1.150	0.5163	0.5163
YDA_ST_21	21	5.669	0.7461	-39.56	-29.48	17.78	17.78	-0.07154	-0.5015	2.337	2.337
YDA_ST_56 rep	56		3.375					2.026	1.596	0.2897	0.2897
YDA_ST_52_5 rep	52.5		3.699					8.558	8.128	0.2660	0.2660
YDA_ST_71_oldertube rep	71	19.90	3.143	-124.5	-114.4	1.550	1.550	10.42	9.994	0.1338	0.1338
YDA_ST_31_5 rep1	31.5		4.095					2.158	1.728	0.3987	0.3987
YDA_ST_31_5 rep2	31.5	12.83	1.023	-35.80	-25.72	6.917	6.917	-14.32	-14.75	0.4700	0.4700
BGH_25_128 rep	128	11.20	3.109	-33.02	-22.94	0.6716	0.6716	-5.050	-5.480	0.1240	0.1240
blank 6		0.1522	0.2184	-33.29				-10.04			
urea R9		5.096	19.01	-39.01		20.38		1.272		46.61	
urea R10		4.803	17.88	-39.34		20.49		1.444		46.64	

Table 4. Second run of $\delta^{13}C$ and $\delta^{15}N$ analysis completed during Fall 2025. Values highlighted indicate unreliable isotope results due to low peak heights. $\delta^{13}C$ and $\delta^{15}N$ values were corrected using an offset determined from urea standards.

Accepted Values

Sample	Meterage	Formation	CO_2 Height (nA)	N_2 Height (nA)	^{13}C Raw	^{13}C Corr	%C Raw	%C Corr	^{15}N Raw	^{15}N Corr	%N Raw	%N Corr
BGH_25_-0_5	-0.5	Beekmantown	1.393	0.2439	-36.22		3.369		-18.92		0.87	
BGH_25_0_4	0.4	New Market	17.52	2.554	-39.98	-29.62	1.105	1.11	-5.325		0.11	
YDA_ST_1_5	1.5	New Market	12.94	7.947	-35.35	-24.99	0.8592	0.86	9.374	9.014	0.33	0.3297
YDA_ST_10_5	10.5	New Market	4.814	2.118	-38.78	-28.42	1.619	1.62	6.706		0.53	
YDA_ST_16_5	16.5	New Market	4.629	1.518	-40.14	-29.78	2.050	2.05	1.580		0.52	
YDA_ST_21	21	Lincolnshire	5.669	0.7461	-39.56	-29.20	17.78	17.78	-0.07154		2.34	
YDA_ST_31_5 rep1	31.5	Lincolnshire		4.095					2.158	1.728	0.40	0.3987
YDA_ST_31_5 rep2	31.5	Lincolnshire	12.83	1.023	-35.80	-25.44	6.917	6.92	-14.32		0.47	
YDA_ST_39	39	Lincolnshire	2.225	0.3315	-45.24		4.294		-18.78		0.92	
YDA_ST_46_5	46.5	Lincolnshire	15.99	1.033	-33.80	-23.44	38.98		2.982		1.69	
YDA_ST_46_5 rep	46.5	Lincolnshire		3.247					2.982	2.552	1.69	1.695
YDA_ST_52_5	52.5	Lincolnshire	9.188	0.9418	-36.14	-25.78	3.306	3.31	7.619		0.31	
YDA_ST_52_5 rep	52.5	Lincolnshire		3.699					8.558	8.128	0.27	0.2660
YDA_ST_56	56	Lincolnshire	10.61	3.375	-36.34	-25.98	6.883	6.88	-5.654	1.596	0.45	0.2897
YDA_ST_60_5 rep	60.5	Lincolnshire	12.47	4.979	-34.94	-24.58	3.190	3.19	19.91	19.55	0.83	0.8255
BGH_25_68_5 rep	68.5	Lincolnshire	12.46	1.053	-34.12	-23.76	1.582	1.58	-6.306		0.11	
YDA_ST_71_newertube	71	Lincolnshire	14.23	1.062	-33.57	-23.21	1.775	1.77	-16.90		0.11	
BGH_25_77	77	Edinburg	11.35	2.586	-32.98	-22.62	0.7173	0.72	-3.065		0.12	
BGH_25_83	83	Edinburg	10.83	3.968	-33.29	-22.93	0.6841	0.68	-1.199	-1.559	0.17	0.1659
BGH_25_89	89	Edinburg	11.88	3.460	-33.63	-23.27	0.7366	0.74	-1.304	-1.664	0.15	0.1474
BGH_94_5	95	Edinburg	14.27	3.441	-33.66	-23.30	0.8610	0.86	-0.9230	-1.283	0.14	0.1416
BGH_25_111_5	111.5	Edinburg	10.16	2.954	-33.15	-22.79	0.6622	0.66	-0.9320	-1.292	0.13	0.1323
BGH_25_116	116	Edinburg	14.67	3.793	-35.55	-25.19	0.8933	0.89	-1.344	-1.704	0.15	0.1544
BGH_25_122	122	Edinburg	14.32	3.959	-33.73	-23.37	0.8709	0.87	-1.699	-2.059	0.16	0.1615
BGH_25_128 rep	128	Edinburg	11.20	3.109	-33.02	-22.66	0.6716	0.67	-5.050	-5.410	0.12	0.1240
BGH_25_134	134	Edinburg	12.78	3.535	-35.66	-25.30	0.8277	0.83	-1.668	-2.028	0.15	0.1543
BGH_25_140	140	Edinburg	12.31	4.013	-33.40	-23.04	0.7679	0.77	-0.9505	-1.310	0.17	0.1671
BGH_25_146	146	Edinburg	15.74	3.567	-33.40	-23.04	1.051	1.05	-2.215	-2.575	0.15	0.1549
BGH_25_152	152	Edinburg	15.83	4.319	-35.61	-25.25	1.008	1.01	-3.287	-3.647	0.18	0.1797
BGH_25_158	158	Edinburg	13.08	4.286	-35.71	-25.35	0.8323	0.83	-0.5949	-0.9549	0.18	0.1764
BGH_25_164	164	Edinburg	11.34	4.336	-35.50	-25.14	0.7043	0.70	-0.0264	-0.3864	0.18	0.1756
BGH_25_170	170	Edinburg	12.69	3.687	-35.74	-25.38	0.7691	0.77	-0.8835	-1.244	0.15	0.1484
BGH_25_179	179	Edinburg	14.88	3.877	-35.49	-25.13	0.9442	0.94	-1.587	-1.947	0.16	0.1620

Table 5. Accepted $\delta^{13}C$ and $\delta^{15}N$ values from carbonate samples, organized by formation and meterage. Sample values were accepted based on CO_2 and N_2 peak heights; low peaks were deemed unreliable. Some samples appear more than once, as $\delta^{13}C$ and $\delta^{15}N$ were measured in separate runs and not always simultaneously. Highlighted values indicate low peak heights or flagged values during processing.

Standards and Correction Factors

^{13}C Urea Raw		%C Urea Raw		^{15}N Urea Raw		%N Urea Raw	
-40.33		20.10		1.351		46.90	
-39.91		19.69		1.537		46.32	
-39.94		19.76		1.456		46.45	
-40.03		19.94		1.460		46.91	
-40.00		19.92		1.459		46.76	
-40.65		20.11		1.301		46.63	
-39.49		20.20		1.388		47.00	
-39.64		19.96		1.604		46.80	
-40.09		20.03		1.555		46.34	
-39.92		20.29		1.673		46.27	
-39.88		20.00		1.682		47.06	
-39.29		19.74		1.720		46.37	
-39.06		19.94		1.698		46.74	
-39.71		20.00		1.658		46.97	
-39.50		20.02		1.685		46.92	
-39.54		19.71		1.683		46.46	
-39.87		19.73		1.686		45.98	
-39.01		20.38		1.272		46.61	
-39.34		20.49		1.444		46.64	
-39.75	Average	**20.00**	Average	**1.543**	Average	**46.64**	Average
0.4167	Stdev	**0.2273**	Stdev	**0.1479**	Stdev	**0.2966**	Stdev
10.36	Offset	**1.000**	Offset	**-0.3626**	Offset	**1.000**	Offset

Table 6. Values of ^{13}C, %C, ^{15}N, and %N from urea standards across both runs. Average values were compared to known true values to calculate offset or scaling correction factors. For δ^{13}C and δ^{15}N, the offset from the true value (−29.39‰ for δ^{13}C and 1.18‰ for δ^{15}N) was used to correct sample values. For %C and %N, correction factors were calculated by dividing the true value (20% for %C, 46% for %N) by the average measured value.

Sample	Meterage	2nd Run	1st Run	2sd	Average
ST-1.5	1.5	-0.26	-0.19	0.076	-0.22
ST-1.5_sub	1.5	-0.19	-0.12	0.066	-0.16
ST-10.5	10.5	-0.54	-0.48	0.058	-0.51
ST-10.5_sub	10.5	-0.48	-0.40	0.076	-0.44
ST-16.5	16.5	-0.36	-0.39	0.031	-0.37
ST-16.5_sub	16.5	-0.29	-0.31	0.024	-0.30
ST-21	21	-0.80	-0.86	0.065	-0.83
ST-21_Sub	21	-0.69			-0.69
ST-31.5	31.5	-0.53	-0.58	0.047	-0.55
ST-31.5_sub	13.5	-0.39	-0.39	0.0027	-0.39
ST-39	39	-0.52	-0.55	0.023	-0.54
ST-39_Sub	39	-0.42	-0.40	0.027	-0.41
ST-46.5	46.5	-0.51	-0.44	0.067	-0.48
ST-46.5_Sub	46.5	-0.39	-0.30	0.086	-0.35
ST-52.5	52.5	-0.56	-0.51	0.046	-0.54
ST-52.5_Sub	52.5	-0.42	-0.35	0.072	-0.38
ST-56	56	-0.55	-0.58	0.032	-0.56
ST-56_sub	56		-0.43		-0.43
ST-60.5	60.5	-0.45	-0.36	0.088	-0.40
ST-60.5_Sub	60.5		-0.20		-0.20

Standard	CRM129	-1.64
	CRM129_Sub	-1.65

Table 7. $\delta^{238}U$ values from the June ICP-MS run, including both blank-subtracted (_Sub) and non-subtracted values for each sample. Two runs were averaged, and 2sd represents the standard deviation of the replicate analyses. Averages are used for data interpretation and plotted in figures. The CRM129 standard and its blank-subtracted counterpart were used for uncertainties.

Sample ID	$\delta^{13}C_{carb}$	$\delta^{18}O_{carb}$
MNE_AJK_JTB_R1	1.847	-8.672
MNE_AJK_JTB_R2	1.831	-8.658
MNE_AJK_JTB_R3	1.870	-8.502
MNE_AJK_JTB_R4	1.896	-8.385
MNE_AJK_JTB_R5	1.887	-8.625
MNE_AJK_JTB_R6	1.920	-8.627
MNE_AJK_JTB_R7	1.664	-8.782
MNE_AJK_JTB_R8	1.756	-8.800
MNE_AJK_JTB_R9	1.580	-8.850
MNE_AJK_JTB_R10	1.626	-8.854
MNE_AJK_JTB_R11	1.744	-8.947
MNE_AJK_JTB_R12	1.738	-8.817
MNE_AJK_MCC_R1	-36.27	-21.89
MNE_AJK_MCC_R2	-35.88	-21.88
MNE_AJK_MCC_R3	-36.18	-21.94
MNE_AJK_MCC_R4	-36.15	-21.85
MNE_AJK_MCC_R5	-36.04	-21.67
MNE_AJK_MCC_R6	-35.87	-21.63
MNE_AJK_MCC_R7	-35.64	-21.57
MNE_AJK_MCC_R8	-35.92	-21.62
MNE_AJK_MCC_R9	-36.08	-21.53
MNE_AJK_MCC_R10	-36.05	-21.72

Standard	$\delta^{13}C$ Average	$\delta^{18}O$ Average	$\delta^{13}C$ STD	$\delta^{18}O$ STD
JTB	1.780	-8.710	0.1131	0.1619
MCC	-36.01	-21.73	0.1845	0.1483

Table 8. $\delta^{13}C_{carb}$ and $\delta^{18}O_{carb}$ values for JTB and MCC standards. Twelve replicates were run for the JTB standard and ten for the MCC standard. Reported averages and standard deviations (STD) are shown in the bottom panel for each standard. The larger of the two standard deviations (between JTB and MCC) was used as the analytical uncertainty for each isotope system. All values are reported relative to the VPDB standard.

Sample	^{139}La	^{140}Ce	^{141}Pr	^{143}Nd
-0.5	2.50	2.99	1.53	1.02
0.4	2.24	1.55	1.05	2.42
1.5	3.64	3.64	2.79	5.02
10.5	8.11	7.10	6.43	4.63
16.5	4.29	5.58	6.08	6.37
21	1.83	5.37	3.12	7.49
31.5	4.37	3.21	5.20	4.95
39	8.29	8.22	6.85	8.33
46.5	4.84	4.36	4.79	3.74
52.5	11.2	10.87	10.4	12.1
56	7.60	8.41	9.78	9.71
60.5	8.83	8.62	9.17	9.37
68.5	10.8	11.2	10.9	12.6
71	13.0	13.1	13.6	13.2
77	8.05	8.33	8.31	8.68
83	32.4	32.5	33.4	33.8
83 rerun	4.69	4.32	5.74	6.22
83 rererun	3.07	2.88	2.65	2.39
89	2.54	1.44	2.11	3.72
95	5.00	5.33	5.56	4.26
111.5	7.07	6.87	6.90	6.88
116	14.8	15.6	15.6	15.6
116 rerun	1.81	0.620	2.17	2.45
122	2.65	2.97	1.96	4.56
128	2.61	3.80	6.46	5.06
134	7.51	6.56	8.66	10.7
134 rerun	4.76	5.20	5.67	6.85
140	4.42	5.37	5.80	5.43
146	5.54	6.08	6.48	5.21
152	11.0	11.8	10.5	10.7
152 re run	3.01	4.98	5.70	6.75
158	6.42	6.36	4.91	5.57
164	6.88	7.12	5.89	6.55
170	8.18	9.58	10.1	9.02
170 re run	5.46	3.04	5.07	0.240
179	7.53	5.62	6.29	7.65
179 re run	2.08	3.29	2.36	2.51

Table 9. Uncorrected raw counts of selected rare earth elements (REEs) measured in carbonate samples. Values represent signal intensities for ^{139}La, ^{140}Ce, ^{141}Pr, and ^{143}Nd, reported in RSD. Multiple reruns were conducted for some samples due to signal inconsistencies. Data have not been blank-subtracted or normalized to internal standards.